https://doi.org/10.5194/egusphere-2025-2952
Preprint. Discussion started: 14 July 2025

Development of A Global 5arcmin Groundwater Model (H08-GMv1.0): Model Setup and Steady-State Simulation

Qing He[1], Naota Hanasaki[1,2], Akiko Matsumura[3], Edwin H. Sutanudjaja[4], Taikan Oki[1]

[1]Department of Civil Engineering, The University of Tokyo, Tokyo, 113-8656, Japan
[2]National Institute for Environmental Sciences, Tsukuba, 305-8506, Japan
[3]Nippon Koei Co. Ltd., Tsukuba, 305-0047, Japan
[4]Department of Physical Geography, Faculty of Geosciences, Utrecht University, Utrecht, the Netherlands

Correspondence to: Qing He (heqing@g.ecc.u-tokyo.ac.jp)

Abstract. Groundwater plays a critical role in regulating the global hydrological cycle and serves as the most stable freshwater resource for human daily water consumption. However, since the in-situ observations are scarce and the global modelling techniques are unmatured, many hydrological models, including H08, a global hydrological model considering human water use activities, downplay the groundwater component, i.e., the underground aquifer is often described as a simple lumped model where no lateral groundwater movement or the water table is represented. Here, we present a global H08-MODFLOW groundwater model (H08-GM), built at a five-arcmin spatial resolution, aiming to enhance the capability of the original H08 model in simulating groundwater flows. We describe the basic model setups and simulations under steady-state conditions in this paper. The sensitivity analyses are first conducted to select the best-performing model run against in-situ observations. All model runs demonstrate overall good performance, with a model-observation correlation coefficient exceeding 0.65. However, the model is more sensitive to aquifer conductivity settings compared to the two previous studies. The best-run steady-state groundwater Water Table Depth (WTD, water table below land surface) shows a consistent geographical pattern with the earlier studies in terms of the geographical pattern, where hallow WTD mainly occurs is predominantly found in humid plains and deep WTD in arid and mountainous regions. We further use the model to examine the mechanisms controlling groundwater flow dynamics and found that the groundwater head distribution generally follows topography, but its local characteristics are regulated by aquifer hydrogeological properties and river-aquifer exchanges, when surface recharge is not a dominant limiting factor. We also present the global cell-to-cell net groundwater lateral flow map and found that the magnitude in some regions is non-negligible to annual groundwater recharge. This highlights the important role of the lateral groundwater flow in maintaining the regional water budget so that it has to be considered in hydrological modeling studies in future. The steady-state simulation from this study provides the necessary initial condition for the transient simulations, which is essentially important to analyze the global groundwater decline trends and will be presented in another paper. The development of the H08-GM model therefore provides a powerful tool for large-scale groundwater studies, which enables direct comparison with other large-scale groundwater models joined the Inter-Sectoral Impact Model Intercomparison Project (ISIMIP), and is essential to advance the development of the next-generation global hydrological models.

https://doi.org/10.5194/egusphere-2025-2952
Preprint. Discussion started: 14 July 2025

1 Introduction

Groundwater plays a critical role in the global hydrological cycle. The water exchange between aquifers and surface water bodies buffers the sharp seasonal fluctuations in river channels and lakes, maintaining the resilience of aquatic landscapes and ecosystems (Jasechko et al. 2021; Huggins et al. 2023; Rhode et al. 2024a, 2024b; Otoo et al. 2025). Such surface-groundwater exchange can also contribute to a significant amount of rainfall and evapotranspiration variability in arid and semi-arid regions (Schaller and Fan 2009; Bierkens and van den Hurk 2007; Condon and Maxwell 2019), therefore mitigating the severity of droughts and heatwaves through land-atmosphere interactions (Maxwell et al; 2007; Kollet and Maxwell. 2008; Keune et al; 2016; Mu et al. 2021); Meanwhile, the groundwater-ocean exchange regulates the ocean salinity and submarine water quality and thus sustains the coastal ecosystem and biodiversity (Luijendijk, Gleeson, and Moosdorf, 2020; Sawyer, David and Famiglietti, 2016; Zhou et al. 2018).

Groundwater serves as a natural freshwater reservoir to supply human water use activities. Due to its large storage capacity and slow flow rate, groundwater contributes as the major and the most stable freshwater source to human water use in households, agriculture, and industry (Wada et al. 2014; Kuang et al. 2024; Gleeson et al. 2012; Scanlon et al. 2023). On a global average, more than 90% of freshwater availability excluding glaciers is contributed by groundwater storage (Magat and van der Gun, 2006). In extremely arid regions where no surface water is available, or during dry seasons when no rainfall recharges surface water bodies, groundwater could be the only water source for the local communities (Gee and Hiller, 1988; Braune and Xu, 2010; Calow et al. 2010). Therefore, understanding the spatial and temporal distribution of groundwater availability is key to addressing water scarcity at local, regional, and global scales.

In the last two decades, three major global hydrological models specifically designed for anthropogenic water use activities (hereafter GHWMs) have been developed, namely, WaterGAP (Döll and Fiedler, 2008; Müller Schmied, H., et al. 2021), PCR-GLOBWB (van Beek and Bierkens 2009; Sutanudjaja, E. H., et al. 2018), and H08 (Hanasaki et al. 2008a, b; 2018). These models have integrated the natural hydrological processes, for example, surface runoff and aquifer storage, as water supply, and human water consumption, such as domestic and industrial water use, as water demand, so as to assess water scarcity at different spatiotemporal scales (Hanasaki et al. 2008b; 2018; 2023; Wada et al. 2011a, 2011b). Such model-based assessments now serve as the foundation for the global water resource evaluations regularly run by the IPCC Assessment Report (e.g., Caretta et al. 2022) and the UNESCO World Water Assessment Program (e.g., The United Nations World Water Development Report 2024).

Yet, a significant shortcoming of the GHWMs is their simplification of the groundwater processes. In the real world, the groundwater flows three-dimensionally, including both vertical flux exchanges with the upper unsaturated zones, and horizontal flows from areas of high hydraulic head to adjacent low-head regions. A purely physical model based on Darcy's

https://doi.org/10.5194/egusphere-2025-2952
Preprint. Discussion started: 14 July 2025

Law, called MODFLOW (McDonald and Harbaugh, 1984; Harbaugh et al. 2000; 2005; Langevin et al. 2021), was developed specifically for three-dimensional groundwater studies two decades before the development of GHWMs. Contemporary successful representations of three-dimensional groundwater lateral flows also include a land surface model ParFlow (Maxwell et al. 2005). However, applying either of them to macro-scale studies requires heavy computational resources. To reduce the computational burden, the first-generation GHWMs chose to only include vertical groundwater exchanges, where the aquifer at each grid is simply modeled as a bucket with no groundwater table or lateral flow between cells. However, the groundwater lateral flows are proven to contribute a substantial amount to the total natural water budget, especially in high spatial resolution studies (Krakauer et al. 2014), and in regions of groundwater convergence and arid climates (de Graaf and Stahl 2022). Such simplification could introduce considerable bias to the models' estimation of total water availability. The absence of explicit representation of the groundwater table also undermines the GHWMs' capability for direct and accurate evaluation of human water withdrawal impact on groundwater depletion, particularly over intensively exploited regions such as Ogallala Aquifer and North China Plain (Scanlon et al. 2012; Cao et al. 2013; Yang et al. 2023).

With the advancements in computational technologies, the representation of lateral groundwater flow in GHWMs has re-invoked interest from the hydrological communities recently (Gleeson et al. 2021; Condon et al. 2021). Among them, benchmark efforts have been made by the PCR-GLOBWB group, where the original bucket groundwater module has been replaced by MODFLOW (Sutanudjaja et al. 2011; 2018; de Graaf et al. 2015; 2017; Verkaik et al. 2024). Noteworthy efforts to address the lateral groundwater flow issues in GHWMs are also seen in the development of WaterGAP 2.0 (Reneicke et al. 2019; Müller Schmied et al. 2021), where a gradient-based global groundwater flow parameterization scheme has been developed and implemented, and a newly developed hydro-economic model CWatM (Burek et al. 2020; Guillaumot et al. 2022). With an explicit groundwater table represented, the current generation of GHWMs is now able to estimate decadal groundwater storage changes and groundwater level declines caused by human water pumping activities, enabling the direct comparison with the observation and estimations from data-driven approaches (de Graaf et al. 2019; Scanlon et al. 2023; Kuang et al. 2024).

Here, we present a global coupled H08-MODFLOW model (H08-GM hereafter) to better represent groundwater lateral flow, thereby improving the realism of simulated groundwater availability and human-groundwater interactions in the original H08. We will first describe the basic model setups, including the coupling framework, parameterization schemes, and the hydrogeological data and in-situ validation data used in this paper. The global 41-year (1979-2019) steady-state simulation results under pristine conditions (i.e., without human groundwater pumping), mainly the spatial distribution of the climatological groundwater depth and aquifer-river channel water flux exchange regime will be included. The steady-state simulation is useful for understanding the long-term balance between recharge and discharge, and provides initial conditions to the transient simulation, which will be discussed in another study. The development of the H08-GM model will allow direct assessments on how lateral flow from adjacent areas can mitigate groundwater decline in highly exploited aquifers, thus aiding

https://doi.org/10.5194/egusphere-2025-2952
Preprint. Discussion started: 14 July 2025

in the evaluation of global water scarcity and informing water management strategies. The explicit representation of the groundwater table in the H08-GM model will also facilitate a more accurate comparison with outputs from other GHWMs that joined the Inter-Sectoral Impact Model Intercomparison Project (ISIMIP).

2 Data and Methods

2.1 General Description: The Coupling Framework

The H08-GM consists of two parts: the surface water processes simulated by H08, and the groundwater processes simulated by MODFLOW. In this section, we provide an overview of how the two models can be connected. Detailed descriptions of the individual models will be given in Sections 2.2 and 2.3, respectively.

Figure 1 shows the coupling framework, where the two models are connected through the water flux exchanges, i.e., at each model grid H08 provides total groundwater recharge, river discharge, and total groundwater withdrawal rate as the hydrological forcing to MODFLOW (red arrows, Figure 1a); Baseflow and groundwater level are then simulated by MODFLOW and outputted back to H08 (grey arrow, Figure 1a). We note that although the two-way coupling is the ideal case to study surface-groundwater interactions, in this study, we only present the offline simulation results (i.e., no feedback from MODFLOW to H08) in order to reduce the computational burden. Both models are built on a 5 arcmin grid to ensure consistent spatial resolution.

2.2 Surface Water Model H08

The H08 model is a global hydrological model considering human water use activities (Hanasaki et al. 2008a, b; 2018). The model considers natural hydrological processes maintaining a closed energy and water balance at each model grid. The soil column is described as a one-layer leaky bucket with a fixed depth of 1m and water draining consecutively at the bottom (subsurface runoff). Soil moisture is obtained through the water balance equation, considering rainfall, snowmelt, evapotranspiration, surface and subsurface runoff, and groundwater baseflow. Evapotranspiration is calculated linearly to the potential evapotranspiration based on a stress factor considering soil moisture. Surface runoff is described as the residual water exceeding soil capacity, while subsurface runoff is calculated as a power function of soil moisture. River discharge is accumulated from surface runoff by the river routing module at each grid. All grid cells within each Köppen climate zone share uniform parameter settings (e.g., soil wilting point and field capacity). Although there is no subgrid distinction between vegetated or bare soil fractions, neither is the soil capillary rise characterized in H08, the simulated hydrological regimes correspond reasonably well to the Budyko aridity framework on a global average (Hanasaki et al. 2008a). Human water infrastructures, including reservoir operations, desalination plants, and inter-basin water transfer through aqueducts and canals, are also available options based on the users' purposes.

https://doi.org/10.5194/egusphere-2025-2952
Preprint. Discussion started: 14 July 2025

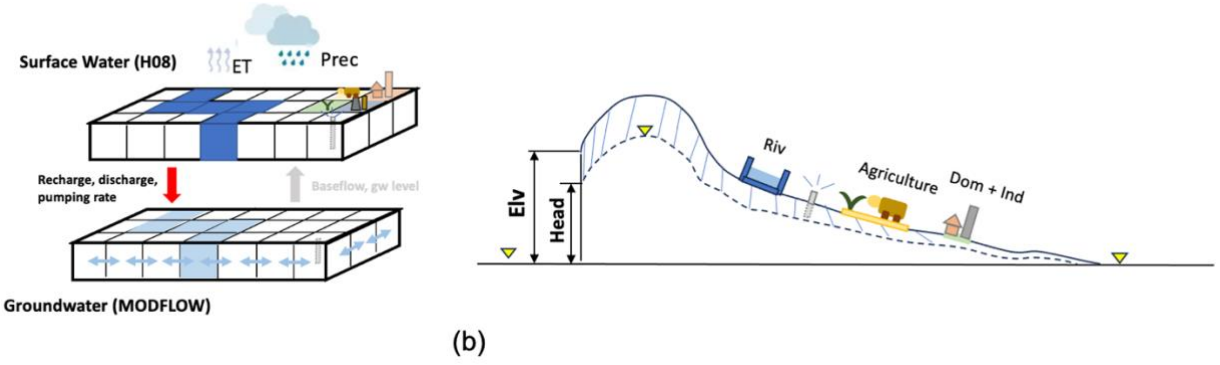

Figure 1. (a) Schematic diagram for H08-GM framework. The upper part of the raster represents the natural hydrological processes, including precipitation, evapotranspiration, river routing, groundwater recharge, and human water withdrawal for different sectors in H08. The lower part of the raster represents groundwater processes, including lateral water flows (shallow blue arrows), aquifer-river water exchanges, and groundwater baseflow. The red arrow indicates hydrological forcing input from surface water (H08) to groundwater (MODFLOW). The grey arrow indicates groundwater feedbacks to surface water. In the current model setting, only the red arrow part is enabled (one-way coupling). (b) Schematic diagram of fundamental processes in groundwater hydrology: land surface elevation (Elv), groundwater head (Head), river–aquifer interaction, and pumping zones. Yellow triangles represent the phreatic surface. The difference between surface elevation and groundwater head is termed as Water Table Depth (WTD).

The groundwater aquifer is described as a single-layer reservoir, where the groundwater storage is accumulated from groundwater recharge that is calculated proportionally to the total runoff (sum of surface and subsurface runoff, Eq. (1)). Since there is no characterization on the aquifer geometry, only the storage changes, rather than the absolute estimation of groundwater storage, are available. The groundwater discharge (baseflow) is calculated as a power function of the groundwater storage accumulation. Two types of aquifers are introduced: renewable and non-renewable. The renewable aquifers can receive water from groundwater recharge, whereas in the non-renewable aquifer, water can only be withdrawn but not replenished. Human water withdrawal is used for three sectors, i.e., household, industry, and agriculture. The total extracted water for agriculture is calculated dynamically based on irrigation water requirement during crop growth, while water withdrawal for the other three sectors is calculated based on the static sectoral water requirement maps provided by AQUASTAT (Food and Agriculture Organization, 2007). The fraction of groundwater use per sector per country from International Groundwater Resources Assessment Centre (IGRAC) database (IGRAC, 2004) is used to determine how much water is abstracted from surface water bodies and how much is from groundwater aquifers. Water abstraction from renewable aquifers has a higher priority than the non-renewable ones. For brevity we only summarize the key elements relevant to this study here, more details are referred to Hanasaki et al. (2008) and Hanasaki et al. (2018).

$$Q_{rc} = \min\left(Q_{rc_{max}}, f_r \cdot f_t \cdot f_h \cdot f_{pg} \cdot Q_{tot}\right), \quad (1)$$

https://doi.org/10.5194/egusphere-2025-2952
Preprint. Discussion started: 14 July 2025

Where, $Q_{rc_{max}}$ is the maximum groundwater recharge (kg m^{-2} s^{-1}), , f_r is a relief-related factor ($0 < f_r < 1$), , f_t is a soil-texture-related factor ($0 < f_r < 1$), , f_h is a hydrogeologyrelated factor ($0 < f_h < 1$), , f_{pg} is a permafrost/glacierrelated factor ($0 <$ fpg < 1), and Q_{tot} is the total runoff (kg m^{-2} s^{-1}). $Q_{rc_{max}}$, f_r, f_t, f_h and f_{pg} are determined by the look-up tables provided in Tables A1–A4 of Döll and Fiedler et al. (2008).

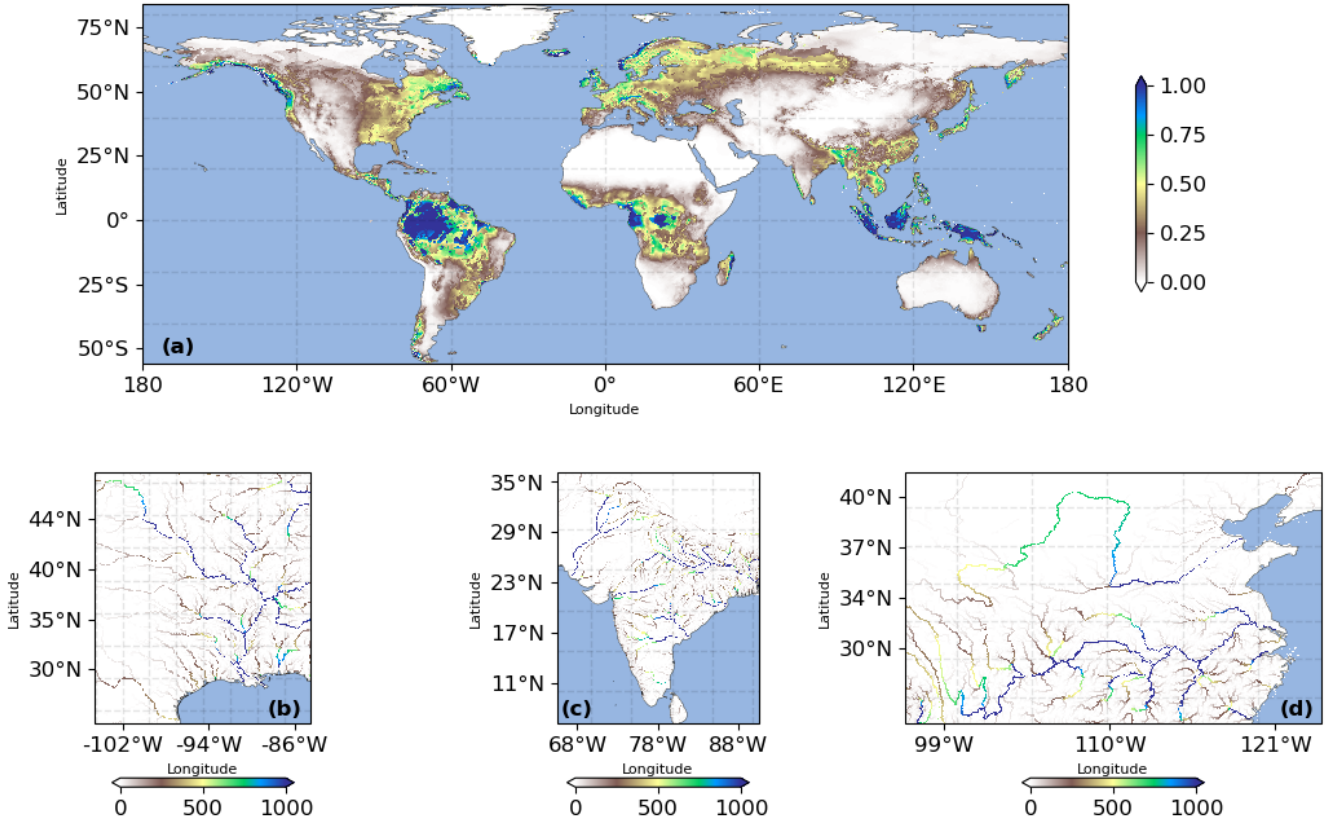

Figure 2. Long-term averaged groundwater recharge and river discharge from H08 (1979-2019). (a) Global distribution of the 41-year averaged groundwater recharge (unit: mm d^{-1}). For a clearer visualization, we show the 41-year mean river discharge (unit: m^3 s^{-1}) in the southern Mississippi River basin (b), the India Peninsula (c), and the Yellow and the Yangtze River basins in China (d), respectively.

We first run H08 individually to obtain the groundwater recharge and river discharge to drive MODFLOW. Global meteorological forcing data including 8 variables, i.e., rainfall, 2 m air temperature, specific humidity, wind speed, surface air pressure, longwave and shortwave radiation, and snowfall, from the W5E5 dataset (Lange et al. 2021) are used. The W5E5 dataset was compiled based on version 2.0 of WATCH Forcing Data methodology applied to ERA5 data (WFDE5; Weedon et al., 2014; Cucchi et al., 2020), ERA5 reanalysis data (Hersbach et al., 2020), and precipitation data from version 2.3 of the Global Precipitation Climatology Project (GPCP; Adler et al., 2003), and was used to support the impact assessments carried

https://doi.org/10.5194/egusphere-2025-2952
Preprint. Discussion started: 14 July 2025

out in phase 3b of the Inter-Sectoral Impact Model Intercomparison Project (ISIMIP3b). The WFDEI data is originally at 0.5 degrees and was post-processed to a 5 arcmin resolution using the linear interpolation function embedded in H08, i.e., the values of the four surrounding grid cells for a certain grid cell will be used to calculate a linear interpolated value by weighting each using the distance ratio. The model was run under the natural scenario at the monthly timestep from January 1, 1979 to December 31, 2019. The results were then aggregated to a monthly step for further analysis. For the steady-state simulation described in this paper, only groundwater recharge and river discharge are used and averaged over the simulation period to obtain the 40-year climatological means. The spatial distributions of these two variables are shown in Figure 2. Groundwater recharge (Figure 2a) is generally higher in humid regions (e.g., the eastern United States, Europe, and southern China) and lower in arid regions (e.g., the western United States, Arabian Peninsula, and inland Eurasia), with maximum values observed in tropical areas such as the Amazon Basin, the Sahel, and the Indonesian archipelago. Figure 2(b)–2(d) shows the spatial distribution of river discharge across representative basins in the United States (lower Mississippi), India (Ganges–Brahmaputra), and China (Yangtze and Yellow Rivers). All three regions show a consistent pattern – the high discharge is mainly concentrated along major rivers and downstream reaches and lower values in upstream or small tributaries. The discharge values are also notably lower under drier climates (Yellow River) compared to other basins under more humid hydro-climatological conditions.

2.3 Groundwater Model MODFLOW

MODFLOW is the USGS's modular hydrologic model for simulating and predicting groundwater conditions (McDonald and Harbaugh, 1984; Langevin et al. 2017). The model uses a generalized control-volume finite-difference approach to solve the two- and three-dimensional groundwater flows based on Darcy's equation. Lateral flows and groundwater heads are explicitly simulated and provided as outputs. The modular structure also allows users to customize the model flexibly by adding packages of their research targets such as aquifer properties, recharge, rivers, and wells, etc. In this study, we use MODFLOW6 (version 6.4.0), to build a global single-layer unconfined groundwater model and replace the original groundwater store in H08. FloPy (Bakker et al. 2016; version 3.3.6) is used as the interface to run the model.

2.3.1 Aquifer Properties

Two aquifer property parameters, i.e., aquifer thickness and hydraulic conductivity, are required to build an unconfined groundwater steady-state model at any spatial scale. Aquifer thickness refers to the vertical extent between the top and bottom boundaries of the aquifer; For a given area, it indicates the aquifer's potential water storage capacity. This parameter is usually obtained from field experiments in local scale studies, while the global map is often delineated based on lithological categories. The GLobal HYdrogeology MaPS (GLHYMPS, Gleeson et al. 2011; 2014; Huscroft et al. 2018) is one pioneering dataset of such a type. However, the GLHYMPS aquifer thickness only accounts for the shallow layer (thickness up to 100m), thus cannot reasonably represent the deep aquifers in the world. A terrain-based approach was then proposed by de Graaf et al. (2015) and proved to be valid for deep aquifer characterization. This approach first generates a random distribution of the

https://doi.org/10.5194/egusphere-2025-2952
Preprint. Discussion started: 14 July 2025

average aquifer thickness based on the land surface and floodplain elevation differences (Δz) at each grid. The optimal guess is then derived by constraining the corresponding log-normal transformation of Δz and a standard normal ordinate function, based on observed statistical values from 6 regional scale studies, where the assumption is that there is similarity in Coefficient of Variations (CV) of aquifer thickness all around the world. In this study, we use aquifer thickness from de Graaf et al. (2015) approach in order to better represent the deep aquifers. The aquifer thickness map is shown in Figure 3(a).

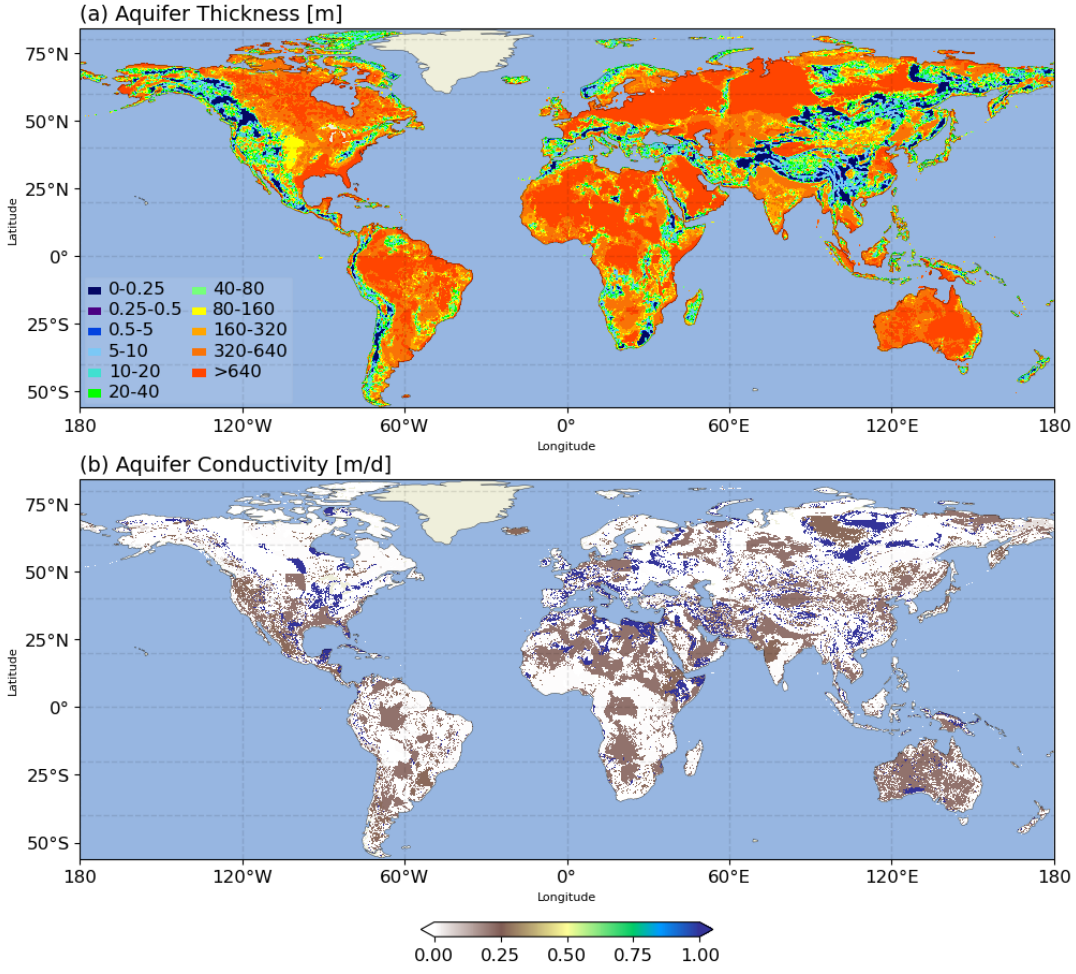

Figure 3. Global distribution of aquifer thickness (a) and aquifer conductivity (b).

Hydraulic conductivity controls the rate at which groundwater flows through the aquifer materials and is primarily determined by the aquifer's lithological characteristics. The gridded 5arcmin GLiM global lithological map (Moosdorf and Hartmann, 2012) is used to define the spatial distribution of 16 lithologies (Figure C1, Appendix). For each lithological category, we obtain the corresponding permeability value from GLHYMPS; when there are multiple values (for subcategories) within one lithology type, we take their means based on the subcategory sample numbers. The standard deviation for each category is also

https://doi.org/10.5194/egusphere-2025-2952
Preprint. Discussion started: 14 July 2025

obtained for the following sensitivity analysis in Section 2.4. The aggregated permeability data for each lithological type is shown in Table B1 (Appendix). The permeability is then converted to hydraulic conductivity as a direct model input.

2.3.2 River Channel Properties (position, level, bottom elevation, riverbed drainage conductivity)

To investigate the river-aquifer exchanges, a river package (RIV) is used. The water flux exchanges are calculated based on the head difference between river channels and the aquifer cells, i.e., water leaks from the river channel to the aquifer when the river water level is higher than the groundwater head and vice versa, as:

$$Q_{flux} = c_{rb} \times (H_{riv} - h_{aq}) \quad (2)$$

Where, H_{riv} and h_{aq} refers to river water level (m) and groundwater head (m), respectively. When the groundwater table is below the river bottom, river bottom elevation (R_{bot}) is used for h_{aq} to limit the maximum water flux exchanges. c_{rb} indicates the riverbed conductance (m^2d^{-1}) and is calculated as:

$$c_{rb} = \frac{RIV_{wth} \times RIV_{len}}{r_{rb}} \quad (3)$$

Where, RIV_{wth} and RIV_{len} are the river channel width (m) and length (m), respectively, both of which are taken from Yamazaki et al. (2011). r_{rb} is the riverbed resistance. In de Graaf et al. (2015), it is taken as 1d. However, in our preliminary analyses we found the simulated head is rather sensitive to this parameter. Therefore, the appropriate value will be selected from several sensitivity experiments. See Section 2.4 for a detailed description.

https://doi.org/10.5194/egusphere-2025-2952
Preprint. Discussion started: 14 July 2025

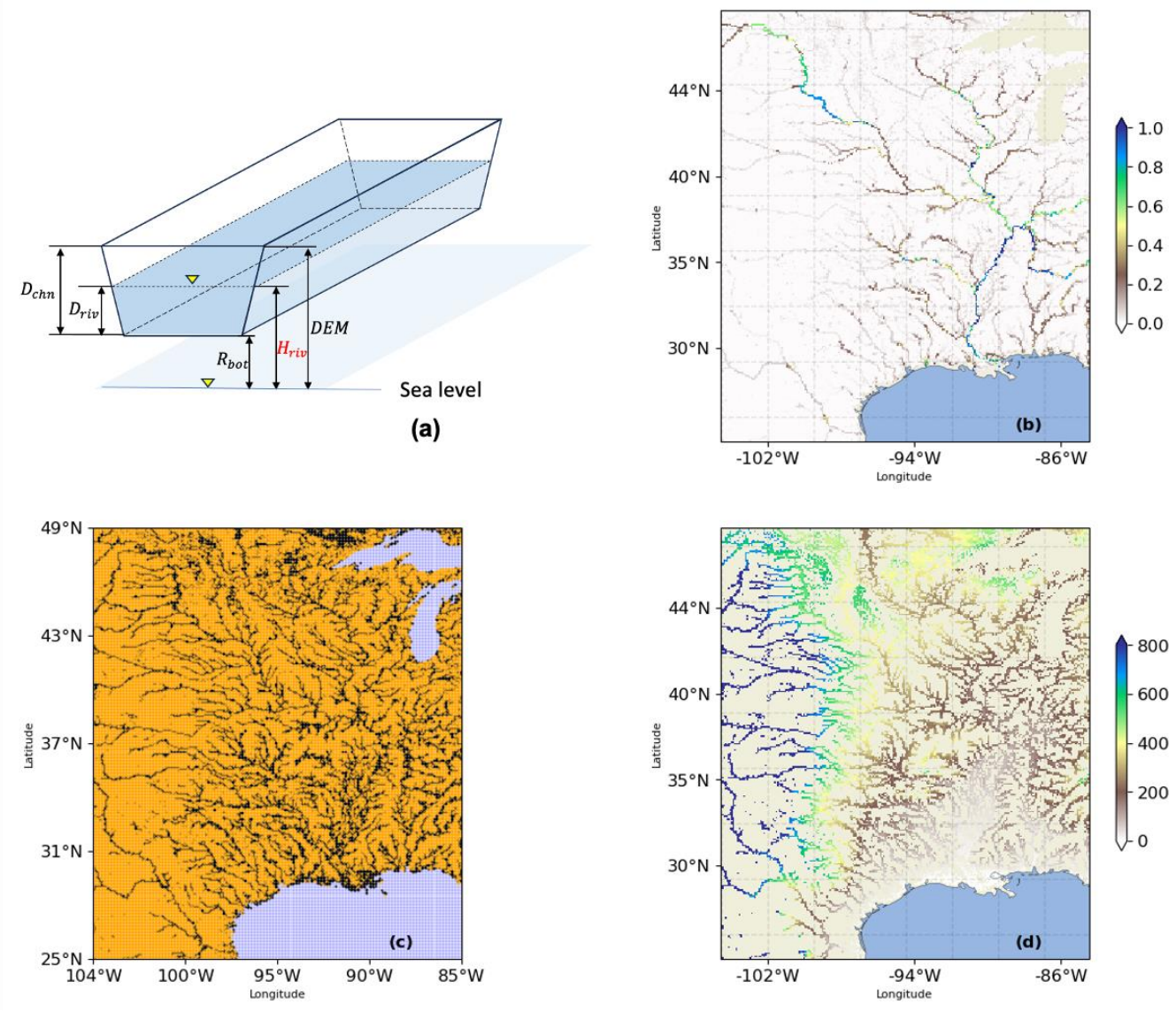

Figure 4. Illustration of the groundwater model grid designations and river properties over the southern Mississippi river basin. (a) Schematic diagram of the river channel geometry. H_{riv} represents the river water level (unit: m) which serves as the input to calculate river-aquifer exchange; (b) Spatial distribution of river width (unit: km) from GWD-LR product (Yamazaki et al. 2014). Data over lake areas are not available; (c) Model designation of MODFLOW. Black, orange, and blue color represents river, drainage, and constant head grids, respectively; (d) Spatial distribution of river water levels (unit: m) calculated from Eq. (4).

We first use a combined satellite and empirical algorithm river width product GWD-LR to allocate the river grids in MODFLOW (Yamazaki et al. 2014). This product was constructed by applying the SRTM Water Body Database (SWBD) and the HydroSHEDS flow direction map, and shows high realism in representing river width for large river channels. To

https://doi.org/10.5194/egusphere-2025-2952
Preprint. Discussion started: 14 July 2025

overcome its limitation in representing small rivers and overestimation of large rivers, we further constrained the results by applying a power-law algorithm, as done in the latest version (v4.20) of the Hydrodynamic flood model CaMa-Flood (Yamazaki et al. 2011). See further description in Text S1 in Supplementary Materials. Because the river-aquifer exchange can be negligible for small tributaries, we define river width larger than 10 m as river grids where water exchanges actually happen, similar to the criteria defined in de Graaf et al. (2015). An illustration of the river width result and the resulting river grid allocation in MODFLOW are shown in Figure 4(b) and (d).

Next, R_{bot} is calculated as the difference between land surface elevation (DEM) and river channel depth (D_{chn}) (Figure 4(a)), where the previous is taken from HydroSHEDS dataset (Lehner et al. 2008), and D_{chn} is calculated based on the power-law algorithm as in CaMa-Flood model (Yamazaki et al. 2011) (Text S1 in Supplementary Materials). H_{riv} is then calculated as:

$$H_{riv} = R_{bot} + D_{riv} \quad (4)$$

Where, D_{riv} is the river water depth (m) and is calculated based on Manning's equation:

$$D_{riv} = \left(\frac{n \times Q_{chn}}{RIV_{wth} \times RIV_{slp}^{0.5}}\right)^{0.6} \quad (5)$$

Where, n is the Manning roughness coefficient and is taken as 0.035 $m^{-1/3}s^{-1}$. RIV_{slp} refers to river channel slope (unitless) and is calculated as the ratio of the DEM difference between the current and next downstream river cells over the distance between the two cells. See Oki and Sud (1998) and Yamazaki et al. (2009) for complete explanations about how the flow direction is decided and the distance between one cell and the next downstream cell is calculated. Q_{chn} refers to the river discharge (m^3/s). For the steady-state simulation in this study, it is calculated as 40yr mean of the monthly H08 simulation. See Figure 2 (b) – (d) for examples of the spatial distribution over southern Mississippi river basin, Indian Peninsula, and Yellow and Yangtze River basin in China.

2.3.3 Other Boundary Conditions (constant head, topography, drainage)

Unlike H08, MODFLOW requires land surface elevation data to calculate groundwater movement. We use DEM from HydroSHEDS for this purpose. For all ocean grids, since the submarine flow is not our research focus, we set them as constant head (CHD) with the water level of 0 m, i.e., it can receive (release) unlimited water from (to) the terrestrial underground aquifer. We also do not separately consider evapotranspiration in the groundwater model because it is already included in the H08 simulation part. For small tributaries (river sequence number less than 10), since the water entering the aquifer system can be negligible, we apply the drainage package (DRN) to allow water to leave the groundwater system. When h_{aq} is above a prescribed level, here set as DEM, water from the groundwater will form ponding areas and be removed from the aquifer system. The drainage rate is calculated based on land surface water conductance, calculated in the same form as Equation (2). No water flux exchange will happen when h_{aq} is below the drainage level (DEM). The allocation for DRN and CHD grids in MODFLOW is illustrated over an example region in Figure 4(c).

https://doi.org/10.5194/egusphere-2025-2952
Preprint. Discussion started: 14 July 2025

Table 1. Sensitivity experiment setting scenarios and the resulting simulation statistics against observations. † Indicates the best-run experiment. For the model and observation difference terms D_{mean} and D_{med}, positive values indicate the overall model head is shallower than observed head and vice versa. D_{std} is always positive; larger values indicate the overall simulated head deviates further from the observation.

	EXP	K	Rch	r_{rb}	R_{cor}	D_{mean}	D_{med}	D_{std}
A	K0R0B0	ref	ref	ref	0.67	452.73	294.50	494.59
	K1R0B0	$+1\sigma$	ref	ref	0.79	271.39	151.58	378.33
	K2R0B0	$+2\sigma$	ref	ref	0.88	34.23	33.16	254.98
	K0R1B0	ref	$+0.5\sigma$	ref	0.53	657.57	445.97	679.84
	K1R1B0	$+1\sigma$	$+0.5\sigma$	ref	0.70	397.78	229.11	505.02
	K2R1B0	$+2\sigma$	$+0.5\sigma$	ref	0.85	89.41	60.37	290.10
	K0R2B0	ref	-0.5σ	ref	0.80	240.32	133.53	334.17
	K1R2B0	$+1\sigma$	-0.5σ	ref	0.85	123.02	63.21	283.00
	K2R2B0	$+2\sigma$	-0.5σ	ref	0.83	-68.97	2.58	297.82
B	K0R0B1	ref	ref	$\times 0.1$	0.95	90.75	65.25	168.20
	K1R0B1	$+1\sigma$	ref	$\times 0.1$	0.95	63.24	41.31	169.67
	K2R0B1	$+2\sigma$	ref	$\times 0.1$	0.93	-24.01	5.70	200.41
	K0R1B1	ref	$+0.5\sigma$	$\times 0.1$	0.94	115.28	87.09	176.19
	K1R1B1	$+1\sigma$	$+0.5\sigma$	$\times 0.1$	0.94	85.86	56.43	175.43
	K2R1B1	$+2\sigma$	$+0.5\sigma$	$\times 0.1$	0.93	1.21	13.08	189.73
	K0R2B1	ref	-0.5σ	$\times 0.1$	0.95	57.86	40.62	165.07
	K1R2B1	$+1\sigma$	-0.5σ	$\times 0.1$	0.94	20.66	22.23	179.68
	K2R2B1	$+2\sigma$	-0.5σ	$\times 0.1$	0.90	-76.61	-6.23	247.28
C	K0R0B2	ref	ref	$\times 0.01$	0.95	47.77	23.72	161.51
	K1R0B2	$+1\sigma$	ref	$\times 0.01$	0.95	30.91	17.35	162.58
	K2R0B2	$+2\sigma$	ref	$\times 0.01$	0.93	-31.23	0.98	193.91
	K0R1B2	ref	$+0.5\sigma$	$\times 0.01$	0.95	51.12	26.85	162.23
	K1R1B2	$+1\sigma$	$+0.5\sigma$	$\times 0.01$	0.95	37.88	21.05	161.85
	K2R1B2†	$+2\sigma$	$+0.5\sigma$	$\times 0.01$	**0.94**	**-18.02**	**4.23**	**184.87**
	K0R2B2	ref	-0.5σ	$\times 0.01$	0.95	36.90	19.35	161.79
	K1R2B2	$+1\sigma$	-0.5σ	$\times 0.01$	0.95	10.53	11.78	172.11
	K2R2B2	$+2\sigma$	-0.5σ	$\times 0.01$	0.92	-51.97	-4.34	211.04

2.4 Sensitivity Analysis

Since uncertainties in the groundwater recharge and key aquifer parameters (i.e., aquifer conductivity and thickness) are reported to be high (Wada et al. 2011; Gleeson et al. 2011, 2014), we conducted several sensitivity analyses to ensure the robustness of the simulated steady-state groundwater head. Additionally, our preliminary analyses show that the river geometry parameters, such as riverbed resistance, can also play an important role in the resulting groundwater head simulation. Therefore, in total, we select 3 parameters, i.e., groundwater recharge RCH, aquifer conductivity K, and riverbed resistance RRB, for sensitivity analyses. The aquifer thickness D is not considered explicitly here because MODFLOW actually applies aquifer transmissivity (KD) for simulation, therefore the effect can be implicitly reflected in the variation in K.

https://doi.org/10.5194/egusphere-2025-2952
Preprint. Discussion started: 14 July 2025

To maintain computational efficiency, for each parameter we did three sensitivity analyses. Together this results in 27 experiments in total (Table 1). We take K0RC0RR0 as the reference experiment, and use Correlation Coefficient (R), Mean, Median, and Standard Deviation of the difference between simulation and observation ($Dmean$, $Dmedian$, $Dstd$) to evaluate the performance of each experiment against observations. For parameters of K and RCH, one and two standard deviations are added individually for each relevant experiment. The statistic for K is from Gleeson et al. (2011) directly, while for RCH it is calculated based on groundwater recharge from H08 monthly simulation output (1979.01 – 2019.12). Note that although the aquifer thickness data we use is for deep aquifers while Gleeson et al. (2011) only provides such information for the shallow, here we assume there is similarity in aquifer thickness statistics between the two layers, similar to the assumption in the derivation of the dataset we use. For RRD, because there is no global reference of how its statistics should look like, rather simplistic scale factors are applied, i.e., 0.1 day and 0.01 day are taken for different experiment settings.

2.5 Validation

To validate the simulation results, we use the equilibrium water table level observations from Fan et al. (2013). In total, this dataset comprises 1,603,781 WTD readings, along with their corresponding elevation and geographic information. We then average the observations within the same model grid cell to mitigate the influence of the point-grid scale gaps as much as possible. Similar to de Graaf et al. (2015), we validate the groundwater head (i.e., surface elevation minus WTD) since it provides a more direct and physically meaningful evaluation fundamental to groundwater flow dynamics. Observations with invalid elevation readings are excluded. The total number of aggregated observations is 75,386.

3 Results and Discussion

3.1 Sensitivity of Simulated Groundwater Head to Hydrogeological Parameters

The statistics of each sensitivity experiment result against observations are shown in Table 1 and Figure 5. The simulation-observation correlation coefficient ranges between 0.66 and 0.95 across experiments ($p < 0.01$), suggesting our model works reasonably well regardless of the different parameter setting scenarios. However, the large difference of the absolute model-observation biases as represented by $Dmean$, $Dmedian$, $Dstd$ suggest that the accuracy of our simulated groundwater head is sensitive to RCH, K and RRD. The reference experiment where no adjustment on the two parameters is made shows the worst performance with three statistics of 452.76 m (D_{mean}), 294.51 m (D_{med}), and 494.59 m (D_{std}), respectively (the lowest R as well, of 0.66). This means the simulated groundwater head is much shallower than the observations. The spatial map of each experiment also reinforces the model's groundwater head overestimation problem (Figures C3 and C4). This may be explained by the water balance at each grid cell: When K is low, the water exchange between adjacent cells is more difficult.

https://doi.org/10.5194/egusphere-2025-2952
Preprint. Discussion started: 14 July 2025

With the amount of water entering each grid cell fixed (unchanged recharge) throughout the simulation, the slower water exchange between cells will result in more water accumulation within the cells and therefore higher water levels.

The model is more sensitive to K compared to other parameters. For instance, in Table 1, when comparing experiments with identical values of RCH and RRD, the simulation biases between experiments with different K values differ by several times, particularly when K is low. This is further seen in the spatial maps in Figure 6 and Figures S3-S4. The simulated groundwater head is more sensitive to K in shallow groundwater areas (blue and green coloured areas, western U.S., Amazon, Sahel, the southern-north Eurasia, etc.) than in areas with deeper water tables (orange and red coloured areas, Rocky and Andes mountains, Tibetan Plateau, etc.). This pattern is consistent with the findings of de Graaf et al. (2015). However, our model's sensitivity to K is notably higher than that reported by de Graaf et al. (2015) and Reinecke et al. (2019). The Coefficient of Variation (CV) of the simulated heads exceeds 0.5 across most regions (not shown). We attribute it to three primary reasons: First, the number of our sensitivity analyses is limited. This may result in amplified standard deviation from individual extreme cases. Second, the model is poorly converged toward equilibrium under low K scenarios, especially in shallow groundwater occurrence regions. As illustrated in Figure 5 (the first column), groundwater heads in many of these areas exceed the drainage level, resulting in surface ponding. This forces us to tune K more favourably toward higher values in the sensitivity analyses, whereas the very low K scenarios stay unexplored. Third, compared to sensitivity analyses in Reinecke et al. (2019), where only $\pm 10\%$ perturbance on K is applied, our experiments feature a broader variability range of K.

The simulated head also shows sensitivity to groundwater recharge RCH and river bed conductance RRD, but the sensitivity is more evident under low K scenarios. For example, the bias differences among the K0R0B0, K0R1B0, and K0R2B0 experiments are significantly larger than those observed in the corresponding experiments within Group A (e.g., K1R0B0, K1R1B0, and K1R2B0) (Table 1). Moreover, in comparison to the corresponding experiments in Group B and Group C, the differences among K0R0B0, K0R0B1, and K0R0B2 biases even show orders of magnitude. These findings indicate that K remains the dominant hydrogeological parameter controlling groundwater head. At the same time, they also suggest that groundwater–surface water interactions—particularly the role of rivers—become crucial in regulating groundwater level fluctuations when lateral groundwater flow into or out of the aquifer system is limited due to low permeability. As a result, the simulation performance gradually improves as K increases; The improvement is further seen when RRD decreases (which means more rapid river-aquifer exchange). To ensure further analyses are based on simulation with the highest realism, we chose the experiment with the best performance against observations as the baseline run (i.e., K2R1B2) for analyses in the following context. We also note that the model's performance could be further improved if more suitable combinations of the parameters were used. This can be achieved through observation-based bias correction procedures such as PEST (Doherty et al. 2003) and SCE-UA (Duan et al. 1992; 1993; 1994). However, since applying these algorithms globally is particularly time-consuming and the concentration of this study is to test the feasibility the established framework, the statistics from the current

https://doi.org/10.5194/egusphere-2025-2952
Preprint. Discussion started: 14 July 2025

best-run experiment are reasonable enough for the time being, therefore we will leave further model improvement in future work.

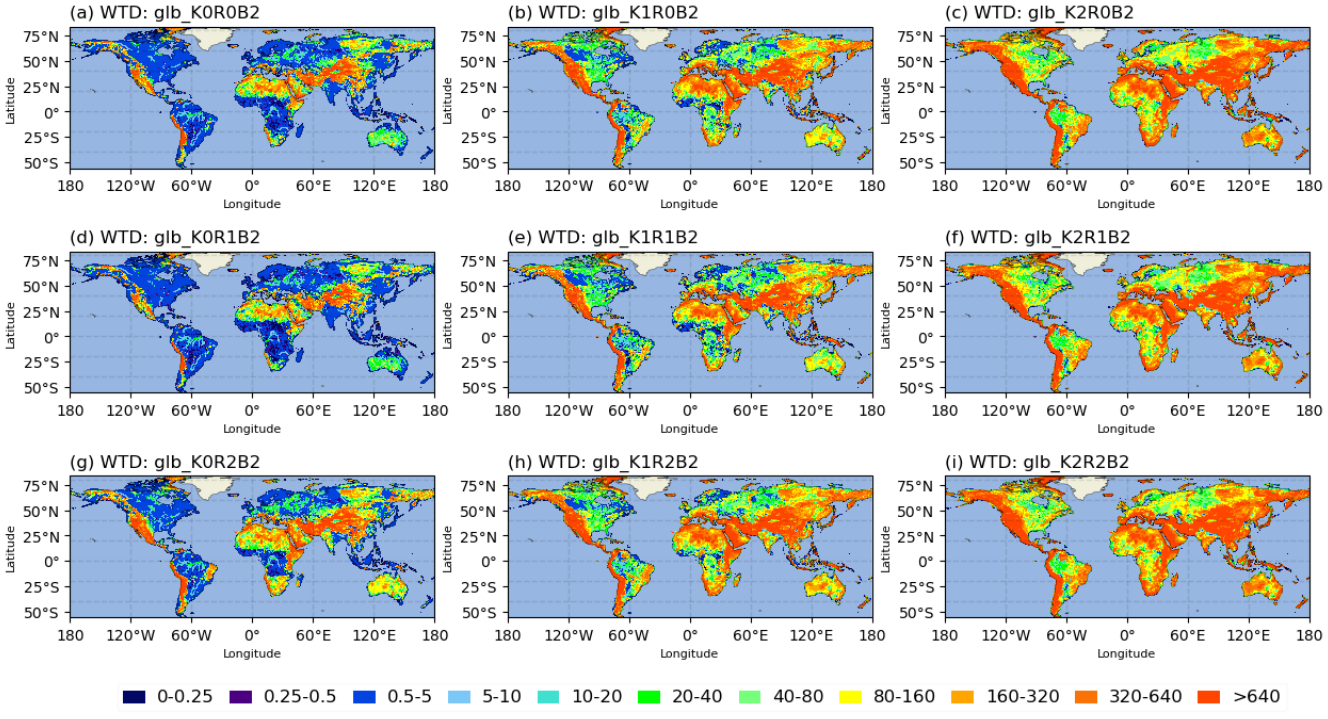

Figure 5. Sensitivity of the simulated WTD to model parameters (Experiment group C).

https://doi.org/10.5194/egusphere-2025-2952
Preprint. Discussion started: 14 July 2025

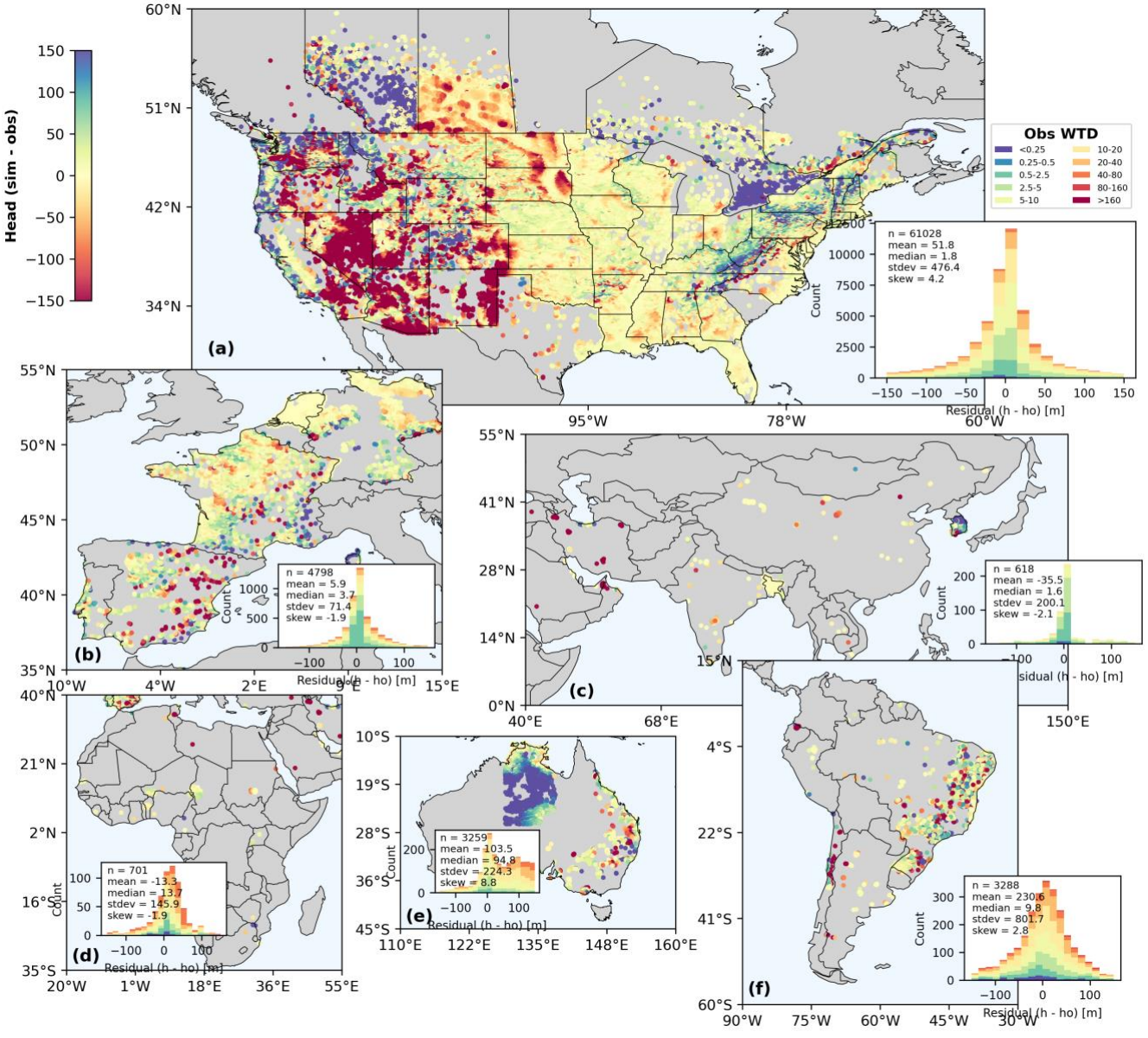

355

Figure 6. Validation of simulated groundwater head against observations over each continent: (a) North America; (b) Europe; (c) Asia; (d) Africa; (e) Australia; and (f) South America. The observed groundwater head is obtained as surface elevation minus WTD, both of which are directly from the report in Fan et al. (2013). Grid cells are masked when either variable is marked as missing value. The missing values mainly concentrate in western Australia (e), which results in a sharp edge in the centre of this region. The inset panels are histograms of the
360 model–observation head residuals (h – ho) over each continent, with bar heights showing the count of sample pairs; the overlaid text annotations indicate the statistics of that residual distribution (mean, median, standard deviation, skewness).

https://doi.org/10.5194/egusphere-2025-2952
Preprint. Discussion started: 14 July 2025

3.2 Simulated Groundwater Head against Observations

Figure 6 shows the spatial maps as well as statistics of the model-observation biases from the best performance run over each continent. For North America where the highest observational density is presented, the model biases show a slightly left-skewed normal distribution. Approximately 47.6% of the analysed grid cells show biases within ±25m and 64.1% within ±50m. These grids are mostly located in the plain-dominated central and south-eastern U.S. The grid cells showing large model-observation biases are distributed mostly over the mountainous areas but in a bimodal way – in the western U.S. the model tends to underestimate the groundwater head whereas in the East the model tends to overestimate it. This can possibly be attributed to the uncertainty in aquifer properties as well as the model's limitation in dealing with sharp groundwater head changes in mountainous areas. Because the topography in the western United States is comparatively higher, and the aquifer thickness is quite shallow (Figure 3(a)), it mainly serves as the divergence region once it receives water from surface recharge. That is, the water will quickly move to adjacent lowlands due to the steep groundwater head gradient. The East, although also elevated, in fact serves as the convergence region due to the deeper aquifer thickness (Figure 3(a)). Over these areas of steep topographic gradient, the model simulation could become quite sensitive to the aquifer conductivity setting. A large K scenario could possibly cause accelerated flow rate (therefore more water loss) in the West. On the contrary, a small K scenario would result in an overestimation of groundwater head in the West, as shown in Figure C5 and Figure C6, where the bias is shown for the experiments glb_K0R1B2 and glb_K1R1B2, respectively. The polarity of biases is rather robust to K scenarios over other areas.

Similar bias distribution is observed for other continents as well. For flatter areas such as the Netherlands and Northern Germany in Europe, Northern China Plain and Bangladesh in Asia, Amazon in South America, the model biases are minimal; whereas for mountainous regions in the Alps and Brazilian Highlands, the model biases are quite pronounced. Nevertheless, the model performs quite optimally in regions with large cities and extensive human activities, which is at the core of our model development purpose – to investigate human-water interactions.

3.3 Global Steady-state Groundwater WTD Map: Best-Performance Run

In Figure 7 we present the global steady-state map of groundwater table depth resulting from the best-run experiment of H08-MODFLOW. The global WTD distribution shows a clear spatial gradient: the groundwater levels are considerably deep over the mountainous and arid regions whereas they remain shallow in flat and humid areas. The result corresponds well with previous studies as in Fan et al. (2013) and de Graaf et al. (2015), and can be explained in the way that the mountains often serve as the divergence place for water to flow out due to their steep topography, and in arid regions the groundwater recharge from the surface is quite limited (vice versa). However, our result corresponds closer to the earlier works of de Graaf et al. (2015) and Reinecke et al. (2019) than that of Fan et al. (2013) which is derived primarily from the observations in which the groundwater depth is up to 100m. Although partly applied the parameterization scheme of aquifer thickness (i.e., the *e*-folding

https://doi.org/10.5194/egusphere-2025-2952
Preprint. Discussion started: 14 July 2025

factor) in Fan et al. (2013), the model framework in Reinecke et al. (2019) largely follows MODFLOW. As such, the large gaps between the numerical and data-driven models here indicate careful comparison in model framework and parameterization schemes is needed to achieve cohesion in the two types of large-scale groundwater modelling studies.

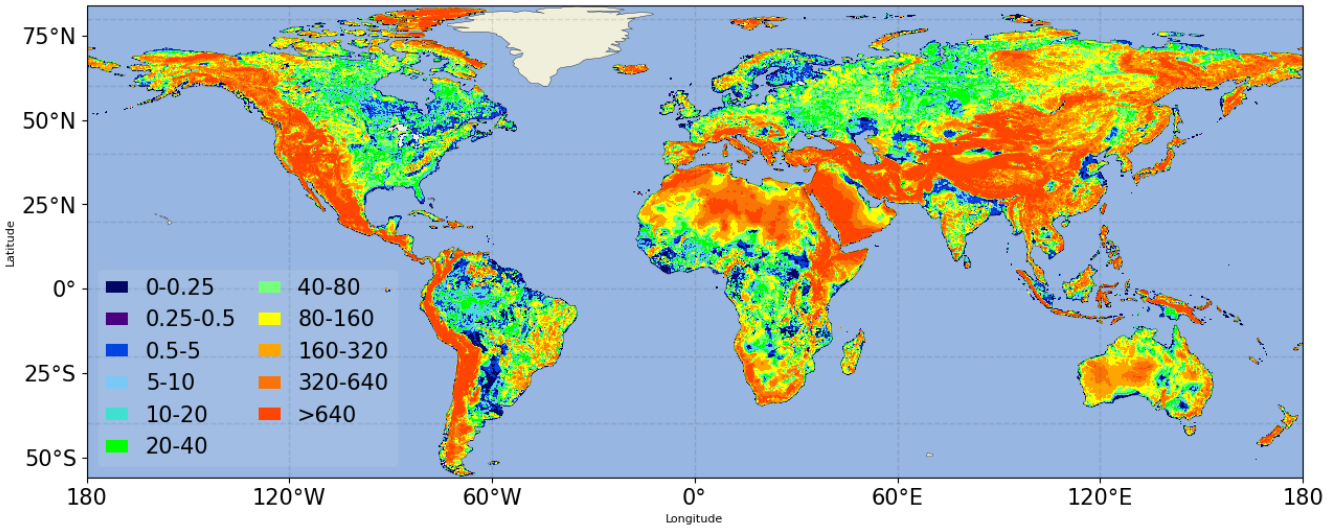

Figure 7. Global best-run steady-state Water Table Depth (WTD, meters below land surface).

3.4 Mechanisms Controlling Groundwater Distribution and Flow Dynamics

To help further understand the groundwater flow dynamics, in Figure 8 we present an analysis of the lower Mississippi River basin to showcase the complex interplays between groundwater flow and topography, aquifer and river hydrogeologic properties, and surface recharge. The high similarity between the spatial pattern of groundwater head and DEM ((Figure 9, (a) and (e)), as well as the flow direction and velocity map (Figure 8(f)), confirms the general principle that groundwater closely follows topography. However, the local characteristics in the north-western part of this region, where steep topography exists but limited groundwater flow present (shown as the low groundwater flow velocity and much deeper groundwater head compared to DEM), suggest aquifer properties that control the hydraulic gradient also play important roles in determining the water movement. The aquifer's K in these areas is much lower than in the other regions (Figure 8(b)), which confirms this finding.

The role of surface recharge is only marginal in this case due to the strong heterogeneity of topography, but is evident in arid climate zones such as in Yellow River basin in Figure C7. The groundwater head distribution is jointly determined by both topography and recharge – in the northwest part of this region, although the topographic gradient is also sharp (Figure C8(a)), the recharge is quite limited (below 0.1 mm d^{-1}) compared to the southeast high area. Consequently, the groundwater head

https://doi.org/10.5194/egusphere-2025-2952
Preprint. Discussion started: 14 July 2025

over the low recharge area is consistently low and shows less spatial heterogeneity, regardless of the topographic gradient which plays an important role in the more humid climate regions.

River properties also play important roles in shaping the local characteristics of the groundwater head distribution through river-aquifer water exchanges. Although the groundwater head in Figure 8(e) appears much smoother than the topography map, we still observe the traces of major river channels, highlighting the significant role of river-aquifer exchange in determining the spatial distribution of the groundwater head. The topography pattern in Figure 8(a) aligns well with the river-aquifer water exchange rate pattern in Figure 8(h): Where there exists substantial water from groundwater to river (red colour), the groundwater head is lower than that in adjacent cells; Whereas where river supplies additional water to the aquifer (blue colour), the groundwater head is higher than the neighbour grid cells. The river-aquifer exchange rate is further determined by riverbed conductance and head difference between groundwater and river water channels. Most grid cells with higher water exchange rate (either positive or negative) tend to have higher riverbed conductance and larger river-groundwater head difference, which corresponds well to the governing equation in Eq. (1). Such river-aquifer exchange pattern is more evident in the Amazon River basins (Figure C8).

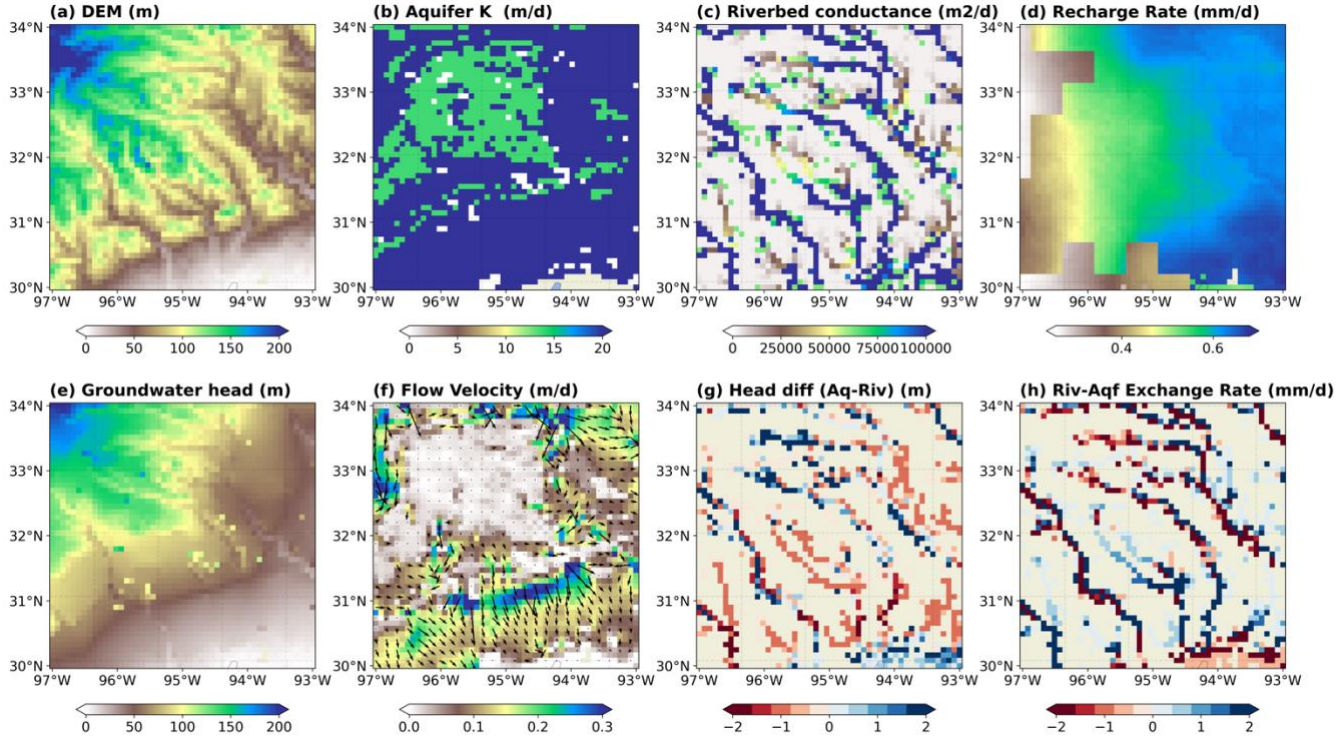

Figure 8. Spatial distribution of key parameters controlling groundwater flow and the resulting surface–groundwater interactions. Panels (a–d) show model input variables, including the digital elevation model (DEM) (a), aquifer hydraulic conductivity (K) (b), riverbed conductance (c), and groundwater recharge rate (d). Panels (e–h) present simulated outputs, including groundwater head (e), lateral flow

https://doi.org/10.5194/egusphere-2025-2952
Preprint. Discussion started: 14 July 2025

velocity with flow directions (f), head difference between aquifer and river (g), and river–aquifer exchange rate (h), where positive values indicate losing rivers (water from rivers to aquifers) and negative values indicate gaining rivers (water from aquifers to rivers). Rectangular in white colour does not indicate missing values but extremely small values.

3.5 Net Groundwater Lateral Flows and Implications for Water Resources Management in Megacities

As one motivation for developing the H08-GM model is to evaluate the compensating effect of groundwater lateral flow on urban water availability, in Figure 9 we also show the 41-year mean steady-state annual net lateral flow flux map. The net lateral flow flux here has the same physical indications as in Krakauer et al. (2014) and de Graaf and Stahl (2022) – the net water fluxes a certain grid cell can gain or lose from the groundwater movement – but is calculated directly from the sum of fluxes at each grid cell's four boundaries, i.e., fluxes through the west, east, south, and north face of each grid cell. The positive values indicate net inflow, that is, the grid cell receives net groundwater inflow from adjacent upstream cells. The grid cell is then defined as groundwater "importers" in this case as in de Graaf and Stahl (2022). Conversely, the negative values of the sum indicate net outflow, which means the grid cell purely loses water to its adjacent downstream cells. Grid cells under this scenario are then defined as groundwater "exporters". Note that the polarity (i.e., the positive or negative sign of the net flux) of the "importers" and "exporters" here is opposite from what is presented in de Graaf and Stahl (2022), since the groundwater net flux in their study is calculated indirectly as the water balance residual of each grid cell, i.e., the sum of recharge, groundwater baseflow, and groundwater storage change. To enable a more straightforward comparison of the groundwater "importers" and "exporters" roles with de Graaf and Stahl (2022), we then reversed the polarity of our results and show them in Figure 10.

The global pattern of groundwater lateral flow from the best-run simulation corresponds reasonably well with both Krakauer et al. (2014) and de Graaf and Stahl (2022), with the highest net lateral flow distributed in Amazon, and moderately high flows in the eastern United States, Central Africa, north-western Eurasia, and the tropical islands. Again, our results compare much closer to de Graaf and Stahl (2022) in magnitude, with the highest flow of more than 600 mm yr^{-1}, much higher than the 100 mm yr^{-1} reported by Krakauer et al. (2014). Similar findings are observed in the way that Amazon serves as the world's largest groundwater exporters, highlighting its critical role in sustaining the ecosystem in its neighbourhood. However, we found that the magnitude of net groundwater lateral flow flux depends heavily on the model's parameter settings (Figure C9, Appendix). When relatively small hydraulic conductivity values are used, the flux magnitude decreases significantly (Figure C9, left column). But still, over the several hotspots in the world, the ratio of net lateral flow flux to groundwater recharge can be

https://doi.org/10.5194/egusphere-2025-2952
Preprint. Discussion started: 14 July 2025

higher than 0.3 even under the lowest hydraulic conductivity scenario, suggesting the lateral groundwater flow plays a nonnegligible role in the grid cell's water budget.

Compared to de Graaf and Stahl (2022), the best-run results (Figure 9 and Figure 10) in our study show a less significant pattern of the global groundwater importers in terms of their magnitude, for example, several regions in southern Amazon, east Tibetan Plateau and the majority of Australia show significant net inflow higher than 60 mm yr^{-1}. However, our results show minimum groundwater net inflows in these areas and show high "importers" characteristics mainly in major river channel grid cells, which may be related to the high river conductance in our model settings. Notably, in de Graaf and Stahl (2022), several heavy groundwater pumping zones, e.g., the Ogallala Aquifer, Indo-Gangetic Plain, and Northern China Plain, are also reported to show high net inflow patterns. This could be true if the human water pumping effect is incorporated, as the pumping cone will create a sharp groundwater gradient that induces net lateral inflows from adjacent areas to compensate for the withdrawal.

Different from the previous study, our results highlight the distinct role of lateral water flow in mainstream river valleys. One may assume the grid cells under mainstream rivers primarily serve as "exporters" due to the high river infiltration. This is not entirely true as we found a large fraction of mainstream river grid cells in Amazon are actually receiving water from upstream (red colour cells in Figure 10 (d)) even though the river water infiltration rate is also high (blue colour cells in Figure C8, (h)). A plausible explanation is that although the river water infiltration can elevate the groundwater head below, this compensating effect may not fully offset the head differences between adjacent cells due to topographic gradients – note that most mainstream rivers are often located in regions of relatively low-elevation. This is demonstrated in Figure C8 (e) that the sharp topographic slope exists between the mainstreams and the adjacent floodplains. On the contrary, the mechanisms for "importers" grid cells in arid climate mainstreams are different. In Yellow River basins (Figure 10 (a)), the groundwater head difference between grid cells is limited (Figure C7(e)) due to the low recharge rate. For the same reason (low recharge), the river water level is low so that the groundwater below the mainstream has to transport water to river channels (Figure C7, (g) and (h)), resulting in a convergence zone where the net lateral flows are positive.

Nevertheless, the net lateral flow results highlight the important role of the compensating effects of groundwater flows in sustaining regional water budgets, which should be considered but have long been downplayed in global water resources management studies. In Figure 9 and Figure 10 we also overlaid several megacities in the world, classified as water-scarce and non-water-scarce categories based on Mekonnen and Hoekstra (2016). It is clearly observed that the groundwater lateral flow effect, whether it be importers or exporters, is quite considerable in some water-scarce cities, e.g., Beijing, Houston, etc., with net groundwater flow higher than 100 mm yr^{-1}. For other non-water-scarce cities as Tokyo, Berlin, New York, etc., the net groundwater flow is even higher, approaching 200 mm yr^{-1}. The large amount of net groundwater flow must be explicitly

https://doi.org/10.5194/egusphere-2025-2952
Preprint. Discussion started: 14 July 2025

incorporated into current water resource management models: Neglecting "exporters" effect may underestimate the city's water stress while neglecting "importers" effect may tend to overestimate it.

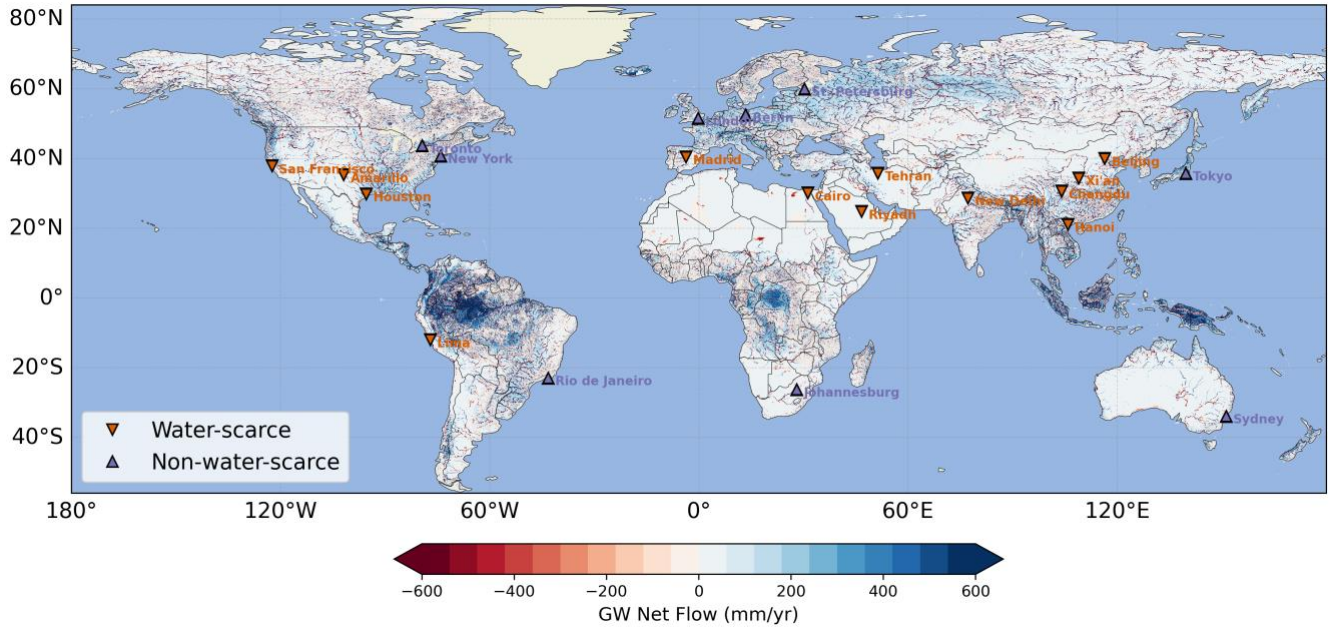

Figure 9. Global distribution of simulated net lateral groundwater flow (mm/yr) derived from the coupled H08-MODFLOW model. Overlaid on the map are major global cities categorized into water-scarce (orange inverted triangles) and non-water-scarce (black upward triangles) groups (Mekonnen and Hoekstra, 2016). Positive values indicate net groundwater flow "exporters" and negative values indicate "importers".

https://doi.org/10.5194/egusphere-2025-2952
Preprint. Discussion started: 14 July 2025

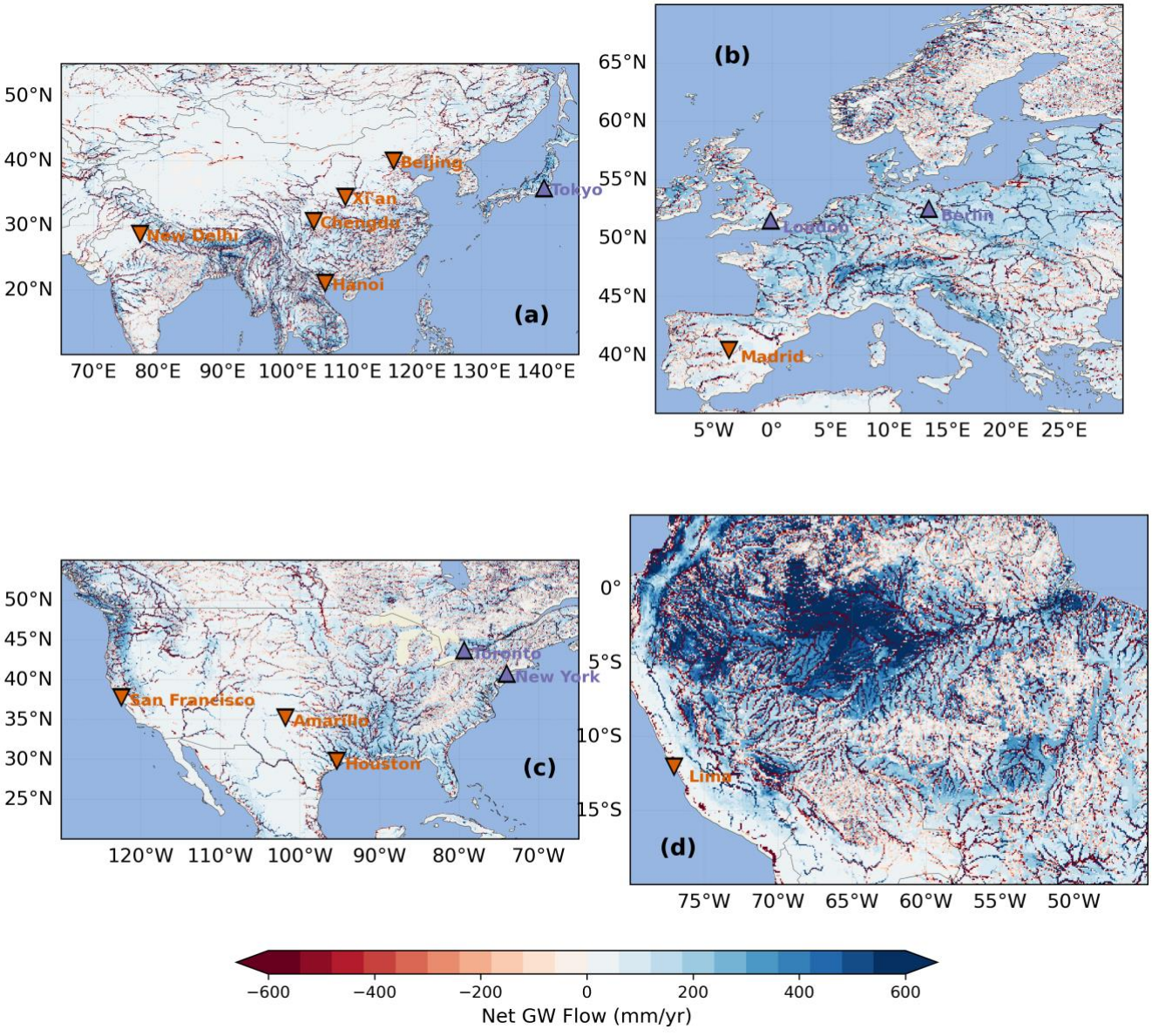

505 **Figure 10.** Same as Figure 9, but zoomed in for different regions.

4 Conclusions

This study has presented a high-resolution global groundwater model H08-GM by incorporating various global hydrogeological datasets. Sensitivity analyses have been conducted on several key model parameters in order to produce the
510 best model performance in simulating the steady-state groundwater levels. Validated against approximately 1.6 million in-situ

https://doi.org/10.5194/egusphere-2025-2952
Preprint. Discussion started: 14 July 2025

observations, the results show that the model with optimal parameter settings performs well at the global scale with R of 0.93. The model performs particularly well over plain areas where large cities and extensive human activities are located, with groundwater head biases within ±25m, but the model tends to show larger biases over mountainous regions, possibly due to the uncertainty in aquifer properties as well as model's limitation in dealing with sharp groundwater head changes. Our results demonstrate that the coupled H08-GM modelling framework can effectively reproduce realistic spatial gradients of groundwater heads, with deeper groundwater tables in mountainous areas from shallower groundwater in plains. Such a pattern primarily results from the topographically driven groundwater flow dynamics, with aquifer and river hydrogeological properties contributing significantly to the local heterogeneity. Using the model, we identify the regions that function as net groundwater "importers" or "exporters" at the global scale and show that the annual net groundwater lateral flow amount can be quite considerable, in the magnitude nonnegligible to annual surface groundwater recharge. This highlights the important role of the groundwater lateral flow in maintaining regional water budget and has to be considered in water resources models, particularly for megacities.

Several limitations should be noted for potential model users. First, our model only applies a single unconfined aquifer layer This simpler model conceptualization was chosen due to the limited availability of global confined aquifer hydrogeological parameters and the evidence that the shallow groundwater (mainly unconfined) contributes largely to sustain anthropogenic and ecological groundwater use purposes (Gao et al. 2018). Second, there still exist uncertainties in the model's key hydrogeological parameters. Compared to the previous research in de Graaf et al. (2015), which includes approximately 1000 Monte Carlo sensitivity experiments, the limited sensitivity analyses in our study may be subject to the degraded confidence of the selected optimal parameter settings. However, the fact that the simulated groundwater heads compare reasonably well to the in-situ observations globally confirms the feasibility of our model, although more comprehensive parameter tunings are suggested in the future.

Our model contributes as one of the three major GHWMs that explicitly considers groundwater lateral flow at the global scale. Additionally, the capability of H08-GM to directly output groundwater levels, calculate lateral flow rate, and connect rivers and aquifers, provides a powerful tool to investigate the groundwater decline trend over the pumping hotspots in the world, to identify river basins as importers or exporters, and to examine the losing and gaining regimes of streamflow. It will essentially help improve the accuracy of the water resource availability estimated based on the original H08 model. The steady-state simulation result in this paper has demonstrated the 40-year mean natural groundwater level distribution without human disturbance. We will show the temporal groundwater level variability and the human water withdrawal effect over the past 40 years in a following paper, which will help further advance our understanding of the important role of groundwater in supporting human water consumption, and the fundamental mechanisms behind the human-groundwater interactions.

https://doi.org/10.5194/egusphere-2025-2952
Preprint. Discussion started: 14 July 2025

Appendix A: Algorithms to calculate river channel depth and river width

In the latest version of CaMaFlood, the river channel depth (D_{chn}) is calculated based on the power-law empirical equation, as:

$$D_{chn} = max\ (H_{min}, H_c * {Q_{chn}}^{H_p} + H_0) \quad \text{(A1)}$$

Where, H_{min}= 1.0 is the prescribed minimum channel depth (unit: m); $H_c = 0.1$ and $H_p = 0.50$ are the coefficients, $H_0 = 0.00$ is the prescribed offset number for river channels; Q_{chn} is the river discharge (unit: $m^3\ s^{-1}$).

The river width (RIV_{wth}) is obtained based on both satellite observation and power-law estimation. The satellite-derived river width is first read in as the baseline variable (RIV_{gwdlr}). The river width based on power-law (RIV_{wth}) is then calculated separately, as:

$$RIV_{wth} = max\ (W_{min}, W_c * {Q_{chn}}^{W_p} + W_0) \quad \text{(A2)}$$

Where, $W_{min} = 5.0$ is the prescribed minimum river channel width (unit: m), $W_c = 2.50$ and $W_p = 0.60$ are the coefficients, and $W_0 = 0.00$ is the prescribed offset number; Q_{chn} is the river discharge (unit: m^3/s).

Afterwards, RIV_{wth} is used to constrain the underestimation of RIV_{gwdlr} for small rivers and overestimation for large rivers, as:

$$RIV_{gwdlr} = \begin{cases} \max(RIV_{gwdlr}, RIV_{wth}), & if\ RIV_{gwdlr} < 50 \\ RIV_{wth} * 0.5, & if\ RIV_{gwdlr} < RIV_{wth} * 0.5 \\ RIV_{wth} * 5.0, & if\ RIV_{gwdlr} > RIV_{wth} * 5.0 \\ 10000, & if RIV_{gwdlr} > 10000 \end{cases} \quad \text{(A3)}$$

https://doi.org/10.5194/egusphere-2025-2952
Preprint. Discussion started: 14 July 2025

565

Appendix B. Look-up table for lithology-based aquifer conductivity (log-transformed, m^2).

The 16 lithology categories are PY (Pycroclastics), VB (Basic Volcanic Rocks), PA (Acid Plutonic Rocks), MT (Metamorphic Rocks), SU (Unconsolidated Sediments), SS (Siliciclastic Sedimentary Rocks), ND (No Data), PB (Basic Plutonic Rocks), SM (Mixed Sedimentary Rocks), WB (Water Bodies), VI (Intermediate Volcanic Rocks), SC (Carbonate Sedimentary Rocks), VA (Acid Vocanic Rocks), EV (Evaporites), PI (Intermediate Plutonic Rocks), IG (Ice and Glaciers). For each lithological categories there are maximum 4 subcategories (SbC). The mean (μ), sample size, and standard deviation (σ) for each subcategory are listed. The category-averaged mean ($\overline{\mu_{logK}}$) and standard deviation ($\overline{\sigma_{logK}}$) are then calculated and given in the last two columns.

Cat	μ_{logK} (m^2)				Sample size (-)				σ_{logK} (m^2)				$\overline{\mu_{logK}}$ (m^2)	$\overline{\sigma_{logK}}$ (m^2)
	SbC1	SbC2	SbC3	SbC4	SbC1	SbC2	SbC3	SbC4	SbC1	SbC2	SbC3	SbC4		
PY	-13.0	-15.2	-12.5	0.0	113	20	33	0	2.0	2.5	1.8	0.0	-13.2	2.0
VB	-12.5	-12.5	0.0	0.0	33	33	0	0	1.8	1.8	0.0	0.0	-12.5	1.8
PA	-14.1	-14.1	0.0	0.0	17	17	0	0	1.5	1.5	0.0	0.0	-14.1	1.5
MT	-14.1	-14.1	0.0	0.0	17	17	0	0	1.5	1.5	0.0	0.0	-14.1	1.5
SU	-13.0	-10.9	-14.0	-13.0	113	82	31	113	2.0	1.2	1.8	2.0	-12.6	1.8
SS	-15.2	-12.5	-16.5	-15.2	20	9	11	20	2.5	0.9	1.7	2.5	-15.0	2.1
ND	N/A	N/A	N/A	N/A	N/A	N/A	N/A	N/A	N/A	N/A	N/A	N/A	-20.0	0.0
PB	-14.1	-14.1	0.0	0.0	17	17	0	0	1.5	1.5	0.0	0.0	-14.1	1.5
SM	-15.2	-12.5	-16.5	-15.2	20	9	11	20	2.5	0.9	1.7	2.5	-15.0	2.1
WB	N/A	N/A	N/A	N/A	N/A	N/A	N/A	N/A	N/A	N/A	N/A	N/A	-20.0	0.0
VI	-12.5	0.0	0.0	0.0	33	0	0	0	1.8	0.0	0.0	0.0	-12.5	1.8

(continued)

https://doi.org/10.5194/egusphere-2025-2952
Preprint. Discussion started: 14 July 2025

(continued)

SC	-11.8	-11.8	0.0	0.0	47	47	0	0	1.5	1.5	0.0	0.0	-11.8	1.5
VA	-12.5	-12.5	0.0	0.0	33	33	0	0	1.8	1.8	0.0	0.0	-12.5	1.8
EV	N/A	N/A	N/A	N/A	N/A	N/A	N/A	N/A	N/A	N/A	N/A	N/A	-20.0	0.0
PI	-14.1	0.0	0.0	0.0	17	0	0	0	1.5	0.0	0.0	0.0	-14.1	1.5
IG	N/A	N/A	N/A	N/A	N/A	N/A	N/A	N/A	N/A	N/A	N/A	N/A	-20.0	0.0

https://doi.org/10.5194/egusphere-2025-2952
Preprint. Discussion started: 14 July 2025

Appendix C: Supplementary figures

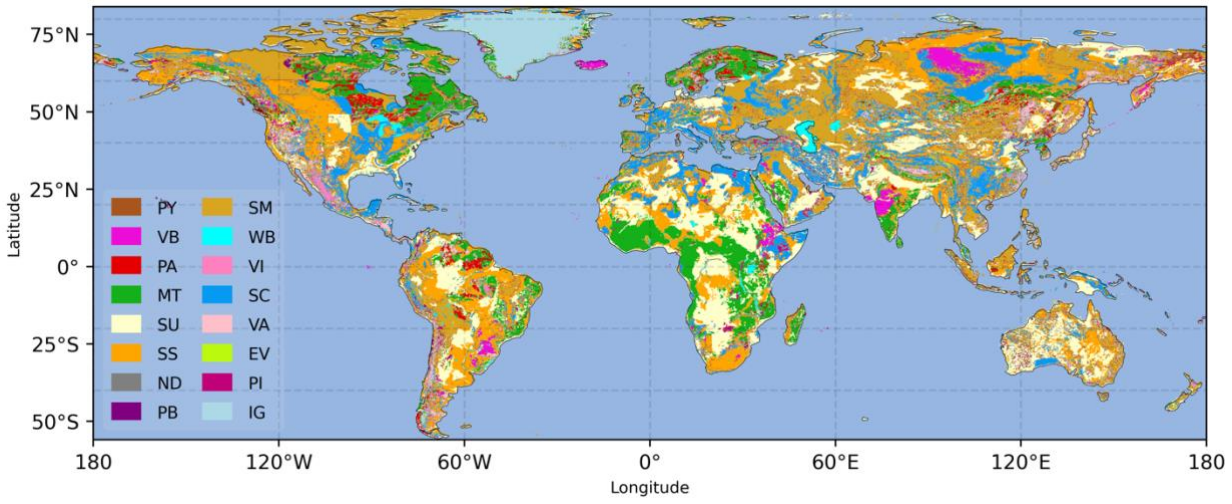

Figure C1. Global distribution of lithology category. The 16 lithology categories are PY (Pycroclastics), VB (Basic Volcanic Rocks), PA (Acid Plutonic Rocks), MT (Metamorphic Rocks), SU (Unconsolidated Sediments), SS (Siliciclastic Sedimentary Rocks), ND (No Data), PB (Basic Plutonic Rocks), SM (Mixed Sedimentary Rocks), WB (Water Bodies), VI (Intermediate Volcanic Rocks), SC (Carbonate Sedimentary Rocks), VA (Acid Vocanic Rocks), EV (Evaporites), PI (Intermediate Plutonic Rocks), IG (Ice and Glaciers).

https://doi.org/10.5194/egusphere-2025-2952
Preprint. Discussion started: 14 July 2025

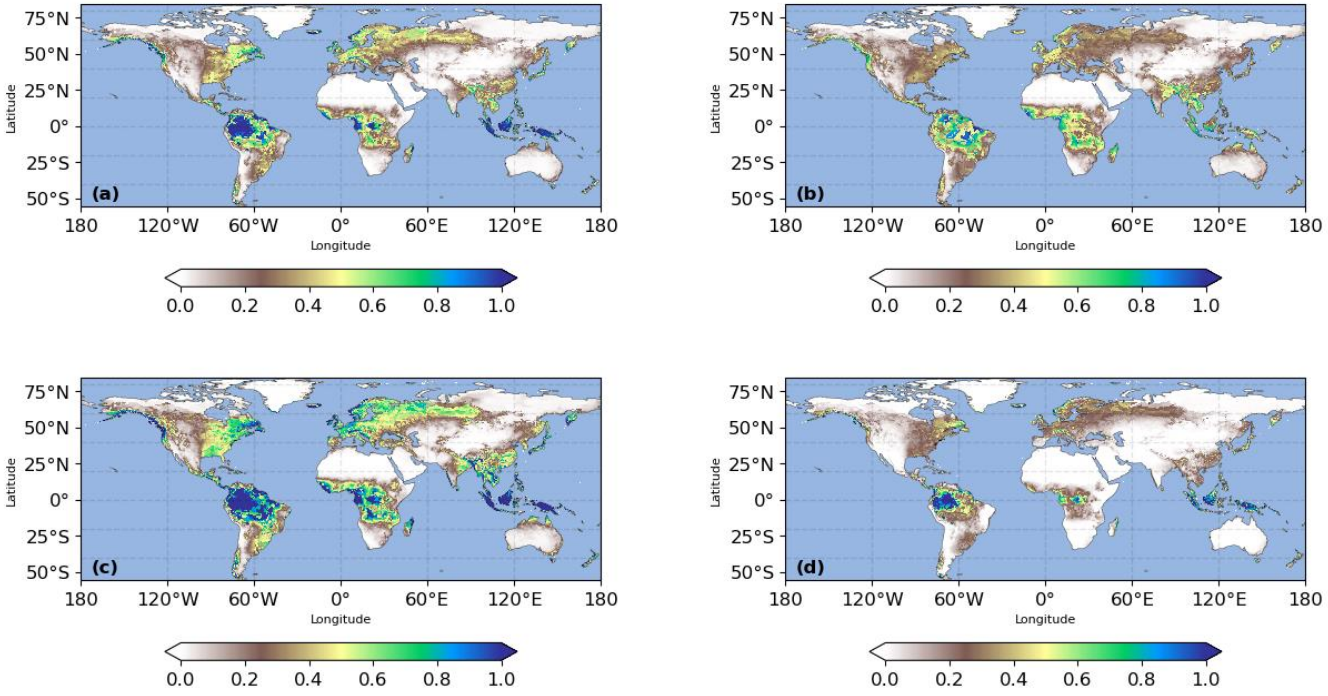

575 **Figure C2** Global distribution of groundwater recharge statistics for sensitivity analyses. (a) Same as Figure 2(a) in the main context: 41-year average groundwater recharge rate (mm d^{-1}); (b) Standard deviation of groundwater recharge rate (mm d^{-1}); (c) Groundwater recharge of 41-year mean plus 0.5 standard deviation (mm d^{-1}); and (d) Groundwater recharge of 40-year mean minus 0.5 standard deviation (mm d^{-1}).

https://doi.org/10.5194/egusphere-2025-2952
Preprint. Discussion started: 14 July 2025

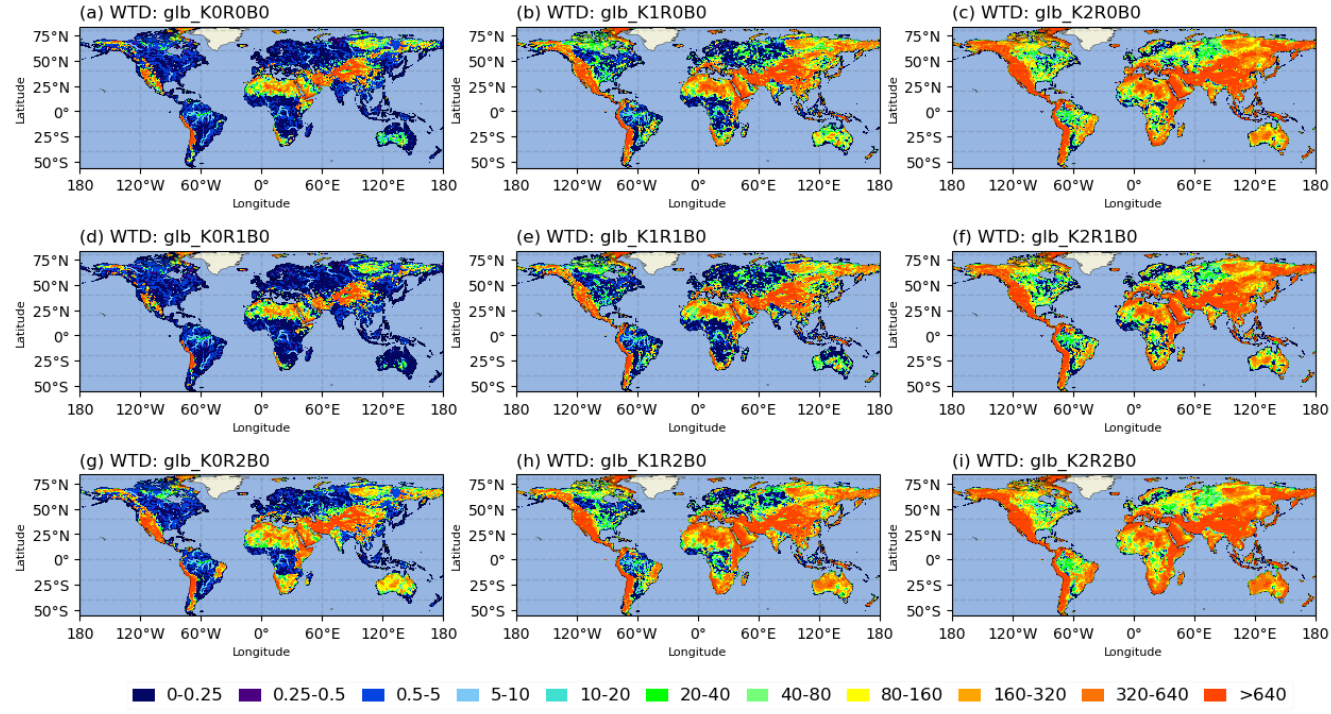

Figure C3. Global WTD distribution from sensitivity experiments Group A

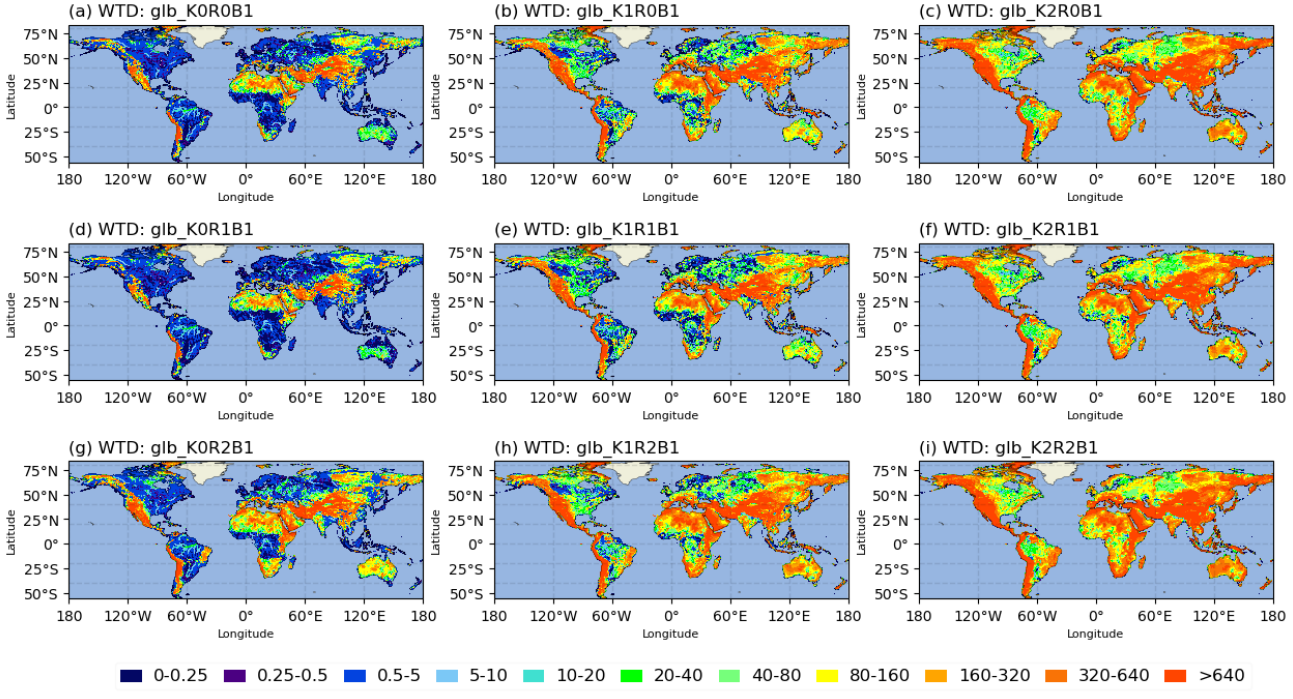

https://doi.org/10.5194/egusphere-2025-2952
Preprint. Discussion started: 14 July 2025

Figure C4 Global WTD distribution from sensitivity experiments Group B

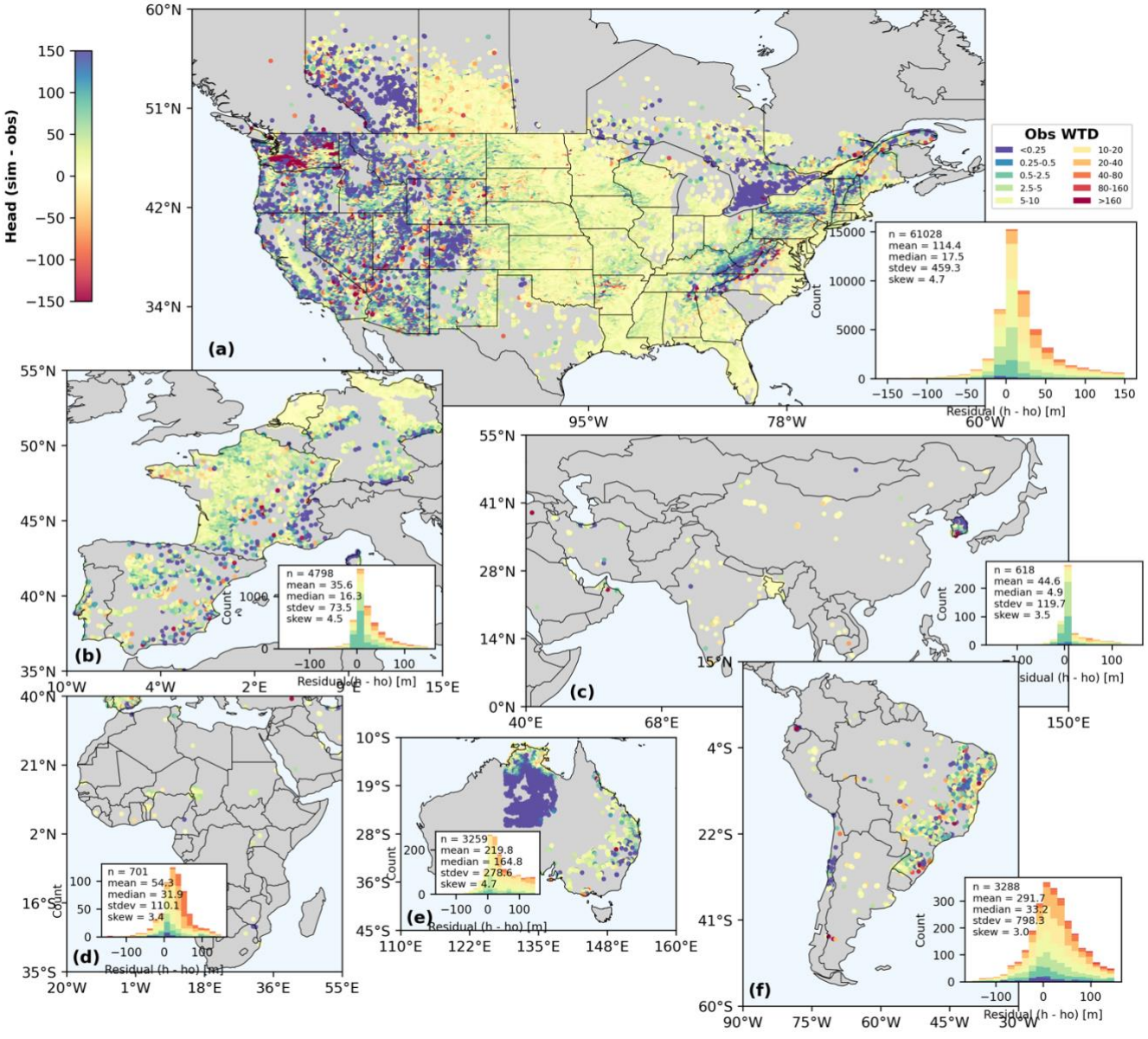

Figure C5 Simulated groundwater head bias from experiment glb_K0R1B2

https://doi.org/10.5194/egusphere-2025-2952
Preprint. Discussion started: 14 July 2025

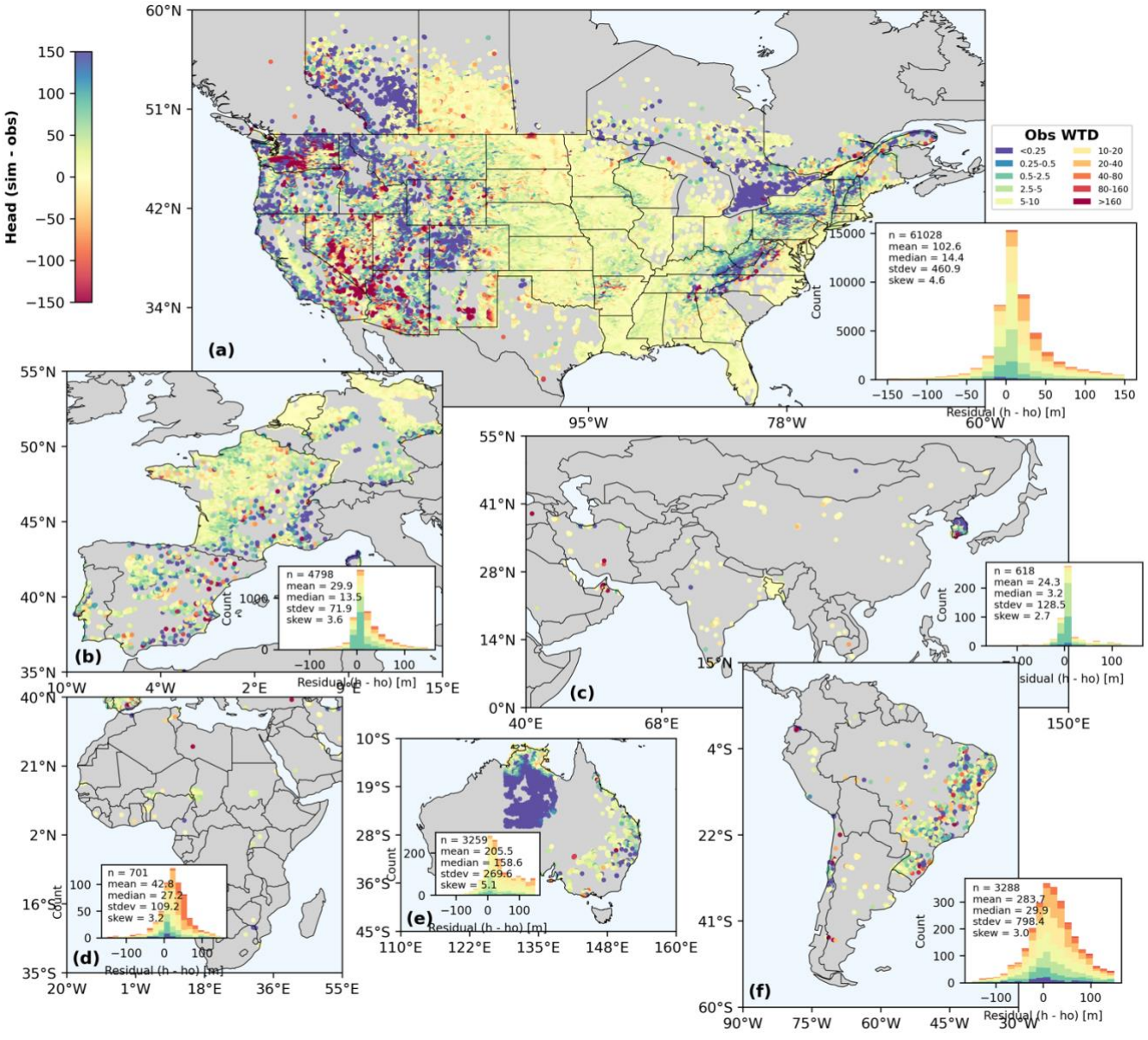

Figure C6 Simulated groundwater head bias from experiment glb_K1R1B2

https://doi.org/10.5194/egusphere-2025-2952
Preprint. Discussion started: 14 July 2025

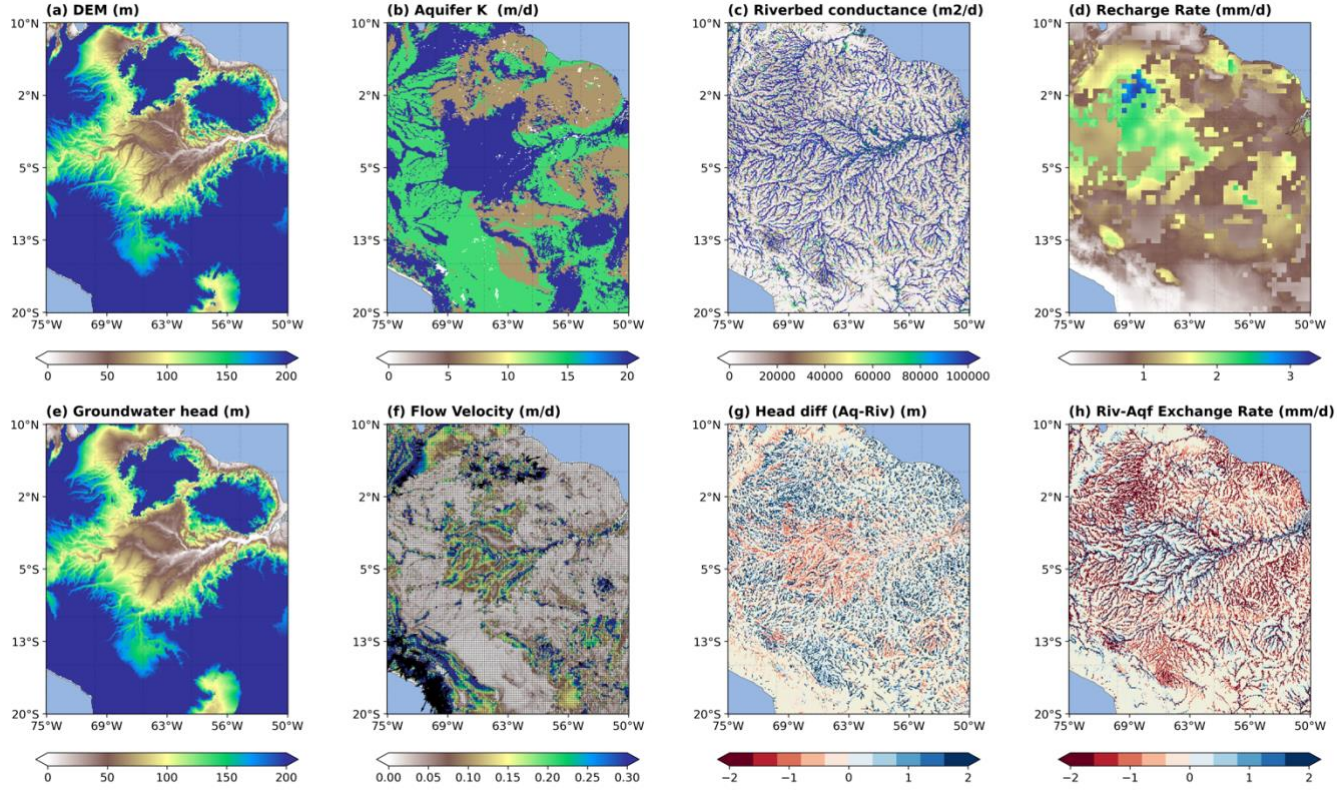

595 **Figure C7** Groundwater flow dynamics in Amazon River basin

https://doi.org/10.5194/egusphere-2025-2952
Preprint. Discussion started: 14 July 2025

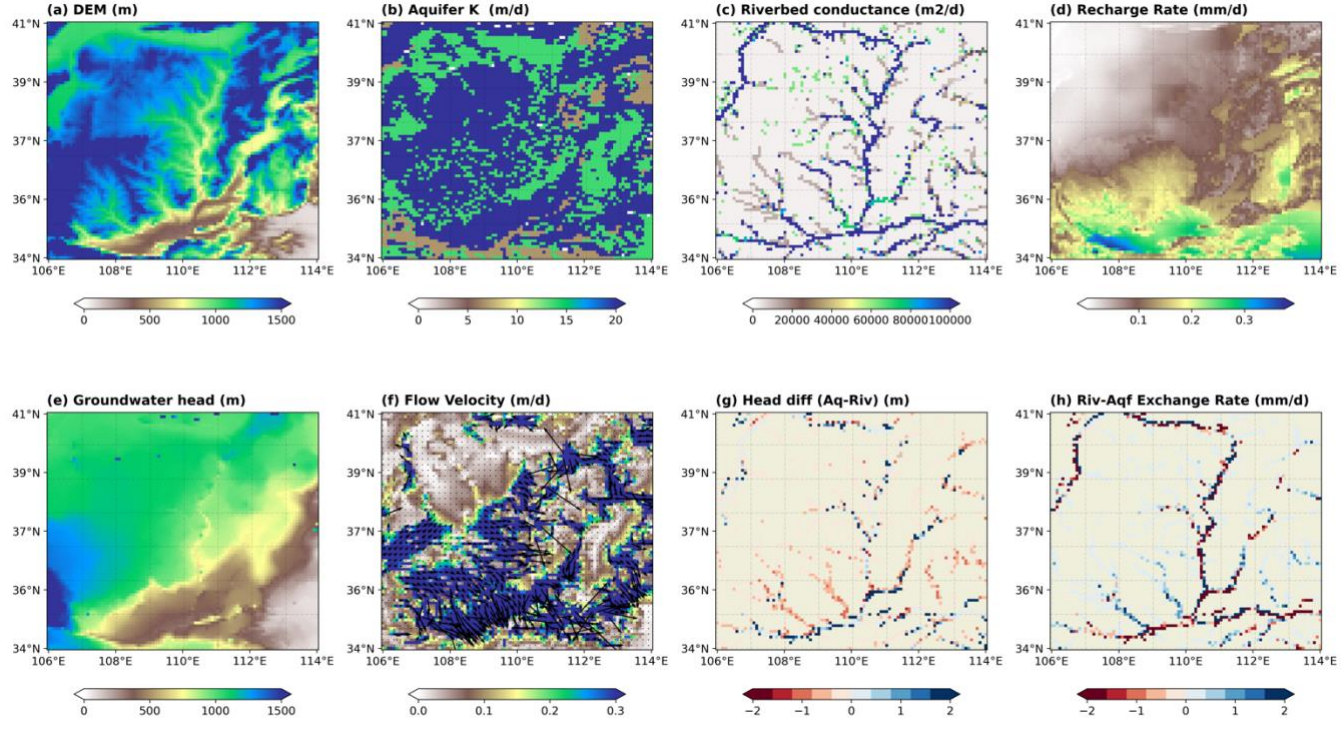

Figure C8 Same as Figure C7, but for Yellow River basin

600

https://doi.org/10.5194/egusphere-2025-2952
Preprint. Discussion started: 14 July 2025

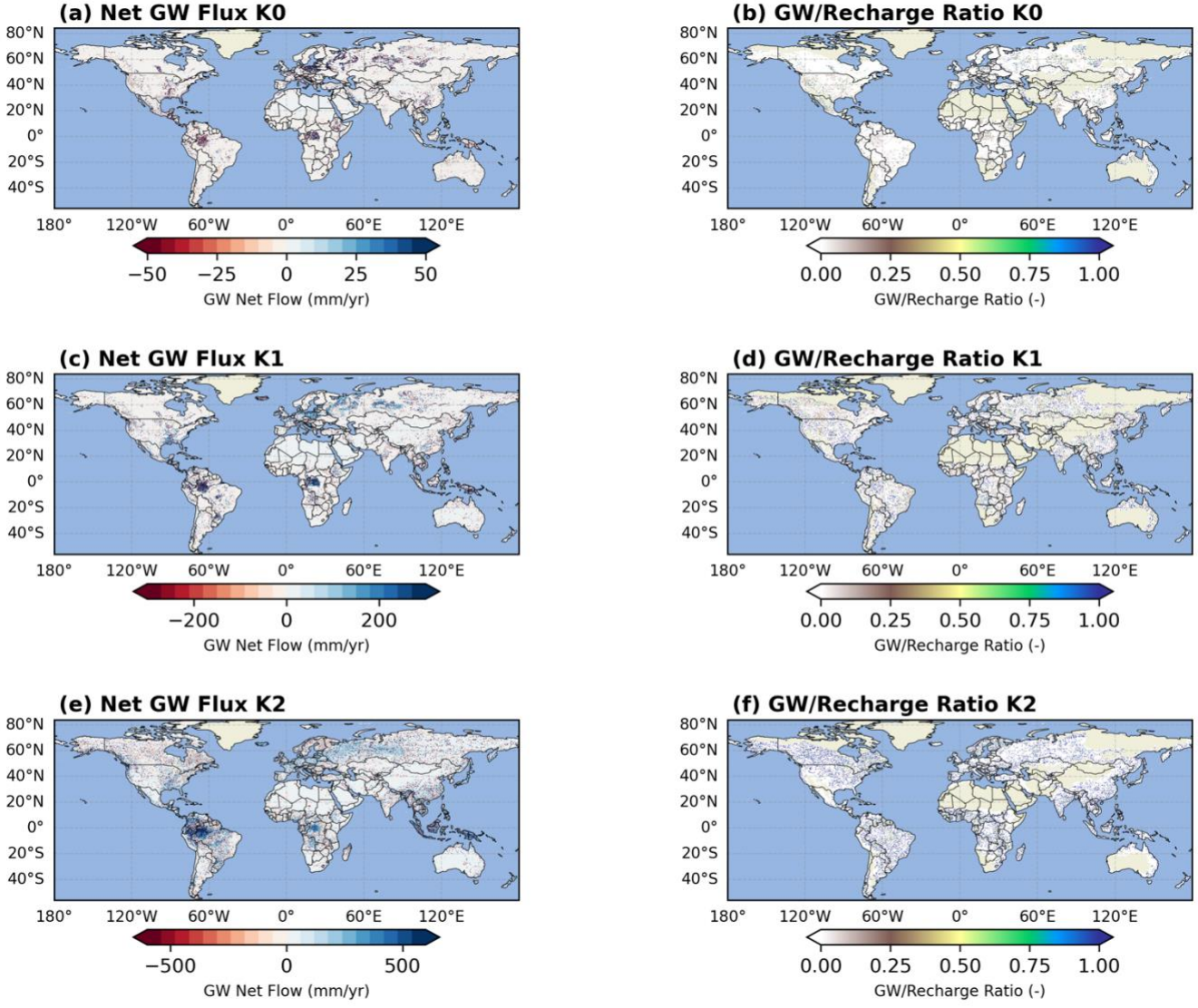

Figure C9 Net lateral flow flux (left column) and ratio of net lateral flow flux to annual groundwater recharge (right column) under different hydraulic conductivity scenarios. K0, K1, and K2 indicates the original hydraulic conductivity, hydraulic conductivity adjusted by one standard deviation, and hydraulic conductivity adjusted by two standard deviations, respectively. Note the colorbar range in the left column is different.

https://doi.org/10.5194/egusphere-2025-2952
Preprint. Discussion started: 14 July 2025

Code and Data Availability

H08-GM v1.0 is open source and distributed under the terms of Creative Commons Attribution 4.0 International License. The development model tools and all data input of H08-GM are available in a Zenodo repository (doi: 10.5281/zenodo.15709184). The development and maintenance of H08-GM are conducted at the Department of Civil Engineering, The University of Tokyo. We welcome researchers from external institutes to contribute.

He, Q., Hanasaki, N., Matsumura, A., Sutanudjaja, E., & Oki, T. (2025). Release of H08-GM(v1.0) code (steady-state). Zenodo. https://doi.org/10.5281/zenodo.15709184

Supplement.

All supplementary materials can be found in Appendix attached in this manuscript.

Author Contributions

QH and NH conceptualized this work. QH performed methodology, implementation for all workflows, pre-processing of hydrogeological data, the simulation of MODFLOW 6, and analyses of the simulation results. AM prepared the global H08 model output. EHS helped with preparation of the aquifer thickness data and several technical issues of MODFLOW simulation. NH and TO supervised this research. QH prepared the manuscript, with contributions from all authors.

Competing Interests.

The contact author has declared that none of the authors has any competing interests.

Acknowledgments

We thank Prof. Ying Fan for providing the global steady-state groundwater head observation data. QH appreciates valuable discussions with Prof. dr. ir. Marc F. P. Bierkens, Dr. ir. Inge de Graaf, Dr. Sida Liu, and other group members during the stay in Utrecht University, as well as the discussions with Prof. Reed Maxwell, Prof. Chunmiao Zheng, and other scientists during the GEWEX groundwater workshop.

https://doi.org/10.5194/egusphere-2025-2952
Preprint. Discussion started: 14 July 2025

Financial Support.

This work was partially supported by Japan Society for the Promotion of Science (KAKENHI; 21H05002) and the Environment Research and Technology Development Fund (JPMEERF23S21120) of the Environmental Restoration and Conservation Agency, Ministry of the Environment of Japan. QH appreciates financial support from JSPS International Research Fellow program (ID No. 24096).

References

Adler, R. F., Huffman, G. J., Chang, A., et al.: The Version-2 Global Precipitation Climatology Project (GPCP) Monthly Precipitation Analysis (1979–Present), Journal of Hydrometeorology, 4(6), 1147-1167, doi:10.1175/1525-7541(2003)004%3C1147:TVGPCP%3E2.0.CO;2, 2003

Bakker, M., Post, V., and Langevin, C. D., et al: Scripting MODFLOW Model Development Using Python and FloPy. Groundwater, 54(5): 733-739, doi: 10.1111/gwat.12413, 2016

Bierkens, M. F. P. and van den Hurk, Bart J. J. M.: Groundwater convergence as a possible mechanism for multi-year persistence in rainfall, Geophysical Research Letters, 34(2): L02402, doi: 10.1029/2006GL028396, 2006

Braune, E. and Xu, Y. The Role of Ground Water in Sub-Saharan Africa, Groundwater. 48(2): 229-238, doi: 10.1111/j.1745-6584.2009.00557.x, 2010.

Burek, P., Satoh, Y., Kahil, T., Tang, T., Greve, P., Smilovic, M., Guillaumot, L., Zhao, F., and Wada, Y.: Development of the Community Water Model (CWatM v1.04) – a high-resolution hydrological model for global and regional assessment of integrated water resources management, Geosci. Model Dev., 13, 3267–3298, https://doi.org/10.5194/gmd-13-3267-2020, 2020.

Calow, R. C., MacDonald, A. M., Nicol, A. L. et al.: Ground Water Security and Drought in Africa: Linking Availability, Access, and Demand, Groundwater, 48(2): 246-256, doi: 10.1111/j.1745-6584.2009.00558.x, 2010

Cao, G., Zheng, C., Scanlon, B. R. et al.: Use of flow modeling to assess sustainability of groundwater resources in the North China Plain, Water Resources Research, 49(1): 159-175, doi: 10.1029/2012WR011899, 2012.

Caretta, M.A., A. Mukherji, M. Arfanuzzaman, R.A. Betts, A. Gelfan, Y. Hirabayashi, T.K. Lissner, J. Liu, E. Lopez Gunn, R. Morgan, S. Mwanga, and S. Supratid: Water. In: Climate Change 2022: Impacts, Adaptation and Vulnerability. Contribution of Working Group II to the Sixth Assessment Report of the Intergovernmental Panel on Climate Change, [H.-O. Pörtner, D.C. Roberts, M. Tignor, E.S. Poloczanska, K. Mintenbeck, A. Alegría, M. Craig, S. Langsdorf, S. Löschke,V. Möller, A. Okem, B. Rama (eds.)]. Cambridge University Press, Cambridge, UK and New York, NY, USA, pp. 551–712, doi:10.1017/9781009325844.006, 2022

Condon, L. E. and Maxwell, R. M.: Simulating the sensitivity of evapotranspiration and streamflow to large-scale groundwater depletion., Science Advances, 5(6): eaav4574, doi: 10.1126/sciadv.aav4574, 2019

Condon, L. E., Stefan, K., Bierkens, M. F. P., et al.: Global Groundwater Modeling and Monitoring: Opportunities and Challenges, Water Resources Research, 57(12), doi: 10.1029/2020WR029500, 2021

https://doi.org/10.5194/egusphere-2025-2952
Preprint. Discussion started: 14 July 2025

Cucchi, M., Weedon, G. P., Amici, A. et al.: WFDE5: bias adjusted ERA5 reanalysis data for impact studies, Earth System Science Data, 12, 2097–2120, doi: 10.5194/essd-12-2097-2020, 2020

de Graaf, I. E. M., Sutanudjaja, E. H., van Beek, L. P. H., and Bierkens, M. F. P.: A high-resolution global-scale groundwater model, Hydrol. Earth Syst. Sci., 19(2): 823-837, doi: 10.5194/hess-19-823-2015, 2015

de Graaf, I. E. M., van Beeek, Rens L. P. H., Gleeson, T., Moosdorf, N., Schmitz, O., Sutanudjaja, E. H., Bierkens, M. F. P.: A global-scale two-layer transient groundwater model: Development and application to groundwater depletion, Advances in Water Resources, 102: 53-67, doi: 10.1016/j.advwatres.2017.01.011, 2017

de Graaf, I. E. M., Gleeson, T., van Beek, L. P. H., Sutanudjaja, E. H., and Bierkens M. F. P.: et al. Environmental flow limits to global groundwater pumping, Nature, 574(7776): 90-94, doi: 10.1038/s41586-019-1594-4, 2019

de Graaf, I. E. M. and Stahl, K: A model comparison assessing the importance of lateral groundwater flows at the global scale, Environmental Research Letters, 17(4): 044020, doi: 10.1088/1748-9326/ac50d2, 2022

Doherty, J. D. (2003). *PEST, a Model-Independent Parameter Estimation Code: User's Manual*. U.S. Army Engineer Research and Development Center, Vicksburg, MS, USA.

Duan, Q., Sorooshian, S., and Gupta, V.: Effective and efficient global optimization for conceptual rainfall-runoff models, Water Resources Research, 28(4): 1015-1031, doi: 10.1029/91WR02985, 1992

Duan, Q., Gupta, V., and Sorooshian, S.: Shuffled complex evolution approach for effective and efficient global minimization, Journal of Optimization Theory and Applications, 76(3): 501-521, doi: 10.1007/BF00939380, 1993

Duan, Q., Sorooshian, S.m and Gupta, V.: Optimal use of the SCE-UA global optimization method for calibrating watershed models, Journal of Hydrology, 158(3-4): 265-284, doi: 10.1016/0022-1694(94)90057-4, 1994

Food and Agriculture Organization: AQUASTAT, available at: http://www.fao.org/nr/water/aquastat/main/index.stm, last access: May 8, 2025

Döll, P. and Fiedler, K.: Global-scale modeling of groundwater recharge, Hydrol. Earth Syst. Sci. 12(3): 863-885, doi: 10.5194/hess-12-863-2008, 2008

Fan, Y., Li. H., and Miguez-Macho, G.: Global Patterns of Groundwater Table Depth, Science, 339(6122): 940-943, doi: 10.1126/science.1229881, 2013

Gao. X., Huo, Z., Xu, X., et al.: Shallow groundwater plays an important role in enhancing irrigation water productivity in an arid area: The perspective from a regional agricultural hydrology simulation, Agricultural Water Management, 208, 43-58, doi: 10.1016/j.agwat.2018.06.009, 2018

Gee, G. W., and Hillel, D.: Groundwater recharge in arid regions: Review and critique of estimation methods, Hydrological Processes, 2(3): 255-266, doi: 10.1002/hyp.3360020306, 1988

Gleeson, T., Smith, L., Moosdorf, N., et al.: Mapping permeability over the surface of the Earth: MAPPING GLOBAL PERMEABILITY, Geophysical Research Letters, 38(2), doi: 10.1029/2010GL045565, 2011

Gleeson, T., Moosdorf, N., Hartmann, J., and van Beek, L. P. H.: A glimpse beneath earth's surface: GLobal HYdrogeology MaPS (GLHYMPS) of permeability and porosity, Geophysical Research Letters, 41(11): 3891-3898, doi: 10.1002/2014GL059856, 2014

Gleeson, T., Wada, Y., Bierkens, M. et al. Water balance of global aquifers revealed by groundwater footprint, Nature 488, 197–200, doi: 10.1038/nature11295, 2012

Gleeson, T., Wagener, T., Döll, P., et al.: GMD perspective: The quest to improve the evaluation of groundwater representation in continental- to global-scale models, Geoscientific Model Development, 14(12): 7545-7571, doi: 10.5194/gmd-14-7545-2021, 2021

https://doi.org/10.5194/egusphere-2025-2952
Preprint. Discussion started: 14 July 2025

Guillaumot, L., Smilovic, M, Burek, P., et al.: Coupling a large-scale hydrological model (CWatM v1.1) with a high-resolution groundwater flow model (MODFLOW 6) to assess the impact of irrigation at regional scale, Geoscientific Model Development, 15(18): 7099-7120, doi: 10.5194/gmd-15-7099-2022, 2022

Hanasaki, N., Kanae, S., Oki, T., et al.: An integrated model for the assessment of global water resources – Part 1: Model description and input meteorological forcing, Hydrology and Earth System Sciences, 12(4): 1007-1025, doi: 10.5194/hess-12-1007-2008, 2008a.

Hanasaki, N., Kanae, S., Oki, T., et al.: An integrated model for the assessment of global water resources – Part 2: Applications and assessments, Hydrology and Earth System Sciences, 12(4): 1027-1037, doi: 10.5194/hess-12-1007-2008, 2008b.

Hanasaki, N., Yoshikawa, S., Pokhrel, Y., et al.: A global hydrological simulation to specify the sources of water used by humans, Hydrology and Earth System Sciences, 22(1): 789-817, doi: 10.5194/hess-22-789-2018, 2018

Hartman, J. and Moosdorf., N. The new global lithological map database GLiM: A representation of rock properties at the Earth surface, Geochemistry, Geophysics, Geosystems, 13(12): 2012GC004370, doi: 10.1029/2012GC004370, 2012

Hersbach, H, Bell, B, Berrisford, P, et al.: The ERA5 global reanalysis. Q J R Meteorol Soc., 146: 1999– 2049, doi:10.1002/qj.3803, 2020

Huggins, X., Gleeson, T., Serrano, D., et al.: Overlooked risks and opportunities in groundwatersheds of the world's protected areas, Nature Sustainability 6, 855–864 (2023), doi:10.1038/s41893-023-01086-9, 2023

Huscroft, J., Gleeson, T., Hartmann, J., et al. : Compiling and Mapping Global Permeability of the Unconsolidated and Consolidated Earth: GLobal HYdrogeology MaPS 2.0 (GLHYMPS 2.0), Geophysical Research Letters, 45(4): 1897-1904, doi: 10.1002/2017GL075860, 2018

International Groundwater Resources Assessment Centre (IGRAC) database. Available at: https://un-igrac.org/data/. Last access: May 8, 2025

Jasechko, S., Seybold, H., Perrone, D., Fan, Y., and Kirchner, J. W.: Widespread potential loss of streamflow into underlying aquifers across the USA, Nature, 591(7850): 391-395, doi: 10.1038/s41586-021-03311-x, 2021

Keune, J., Gasper, F., Goergen, K. et al.: Studying the influence of groundwater representations on land surface-atmosphere feedbacks during the European heat wave in 2003, Journal of Geophysical Research: Atmospheres, 121(22), doi: 10.1002/2016JD025426, 2016

Kollet, S. and Maxwell., R. M.: Capturing the influence of groundwater dynamics on land surface processes using an integrated, distributed watershed model: INFLUENCE OF GROUNDWATER DYNAMICS ON LAND, Water Resources Research, 44(2): doi: 10.1029/2007WR006004, 2008

Krakauer, N. Y., Li, H., and Fan, Y.: Groundwater flow across spatial scales: importance for climate modeling, Environmental Research Letters, 9(3): 034003, doi: 10.1088/1748-9326/9/3/034003, 2014

Kuang, X., Liu, J., Scanlon, B. R. et al.: The changing nature of groundwater in the global water cycle, Science, 383(6686): eadf0630, doi: 10.1126/science.adf0630, 2024

Lehner, B., Verdin, K., and Jarvis, A.: New Global Hydrography Derived From Spaceborne Elevation Data, Eos, Transactions American Geophysical Union, 89(10): 93-94, doi: 10.1029/2008EO100001, 2008

Luijendijk, E., Gleeson, T., and Moosdorf, N. Fresh groundwater discharge insignificant for the world's oceans but important for coastal ecosystems, Nature Communications, 11(1): 1260, doi: 10.1038/s41467-020-15064-8, 2020

Magat, M., & van der Gun, J. (2006). Groundwater around the world. CRC Press.

Maxwell, R. M. and Miller, N. L.: Development of a Coupled Land Surface and Groundwater Model, 6(3): 233-247, Journal of Hydrometeorology, doi: 10.1175/JHM422.1, 2005

https://doi.org/10.5194/egusphere-2025-2952
Preprint. Discussion started: 14 July 2025

Maxwell, R. M., Chow, F. K., and Kollet, S.: The groundwater–land-surface–atmosphere connection: Soil moisture effects on the atmospheric boundary layer in fully-coupled simulations, Advances in Water Resources, 30(12): 2447-2466, doi: 10.1016/j.advwatres.2007.05.018, 2007

McDonald, M. G. and Harbaugh, A. W.: A modular three-dimensional finite-difference ground-water flow model (U.S. Geological Survey Techniques of Water-Resources Investigations, Book 6, Chapter A1). U.S. Geological Survey. 1984

Mekonnen, M. M. and Hoekstra, A. Y.: Four billion people facing severe water scarcity, Science Advances, 2: e1500323, doi: 10.1126/sciadv.1500323, 2016

Mu, M., De Kauwe, M. G., Ukkola, A. M., Pitman, A. J., Guo, W., Hobeichi, S., and Briggs, P. R.: Exploring how groundwater buffers the influence of heatwaves on vegetation function during multi-year droughts, Earth Syst. Dynam., 12, 919–938, https://doi.org/10.5194/esd-12-919-2021, 2021.

Harbaugh, A. W., Banta, E. R., Hill, M. C., & McDonald, M. G. (2000). *MODFLOW-2000, the U.S. Geological Survey modular ground-water model—User guide to modularization concepts and the Ground-Water Flow Process* (U.S. Geological Survey Open-File Report 00–92). U.S. Geological Survey

Harbaugh, A. W. (2005). *MODFLOW-2005, the U.S. Geological Survey modular ground-water model—The Ground-Water Flow Process* (U.S. Geological Survey Techniques and Methods 6–A16). U.S. Geological Survey.

Lange, S., Menz, C., Gleixner, S., Cucchi, M., Weedon, G. P., Amici, A., Bellouin, N., Müller Schmied, H., Hersbach, H., Buontempo, C., Cagnazzo, C.): WFDE5 over land merged with ERA5 over the ocean (W5E5 v2.0). ISIMIP Repository. Doi: 10.48364/ISIMIP.342217, 2021

Langevin, C. D., Hughes, J. D., Banta, E. R., Niswonger, R. G., Panday, S., & Provost, A. M. (2021). *MODFLOW 6—U.S. Geological Survey Modular Hydrologic Model version 6.3.0: Groundwater Flow Model* (U.S. Geological Survey Techniques and Methods 6–A55). U.S. Geological Survey. https://doi.org/10.3133/tm6A55

Müller Schmied, H., et al.: The global water resources and use model WaterGAP v2.2d: model description and evaluation, Geosci. Model Dev., 14, 1037–1079, doi: 10.5194/gmd-14-1037-2021, 2021

Oki, T. and Sud, Y.C.: Design of Total Runoff Integrating Pathways (TRIP)—A Global River Channel Network, Earth Interactions. 1(1): 1-37, doi: 10.1175/1087-3562(1998)002<0001:DOTRIP>2.3.CO;2, 1998

Otoo, N. G., et al.: Mapping groundwater-dependent ecosystems using a high-resolution global groundwater model, Hydrol. Earth Syst. Sci., 29, 2153–2165, https://doi.org/10.5194/hess-29-2153-2025, 2025.

Reinecke, R., Foglia, L., Mehl, S., Trautmann, T., Cáceres, D., and Döll, P.: Challenges in developing a global gradient-based groundwater model (G3M v1.0) for the integration into a global hydrological model, Geosci. Model Dev., 12, 2401–2418, doi: 10.5194/gmd-12-2401-2019, 2019.

Rhode et al.: Groundwater-dependent ecosystem map exposes global dryland protection needs, Nature, 632(8023): 101-107, doi: 10.1038/s41586-024-07702-8, 2024

Rohde, M.M., et al.: Establishing ecological thresholds and targets for groundwater management. Nat Water 2, 312–323, doi: 10.1038/s44221-024-00221-w, 2024

Sawyer, A.H., David, C.H., Famiglietti, J.S. Continental patterns of submarine groundwater discharge reveal coastal vulnerabilities. Science. 353(6300): 705-707, doi: 10.1126/science.aag1058, 2016

Scanlon, B.R. et al.: Groundwater depletion and sustainability of irrigation in the US High Plains and Central Valley, Proceedings of National Academy of Science, 109 (24), 9320-9325, doi: 10.1073/pnas.1200311109, 2012

Scanlon, B.R., Fakhreddine, S., Rateb, A. et al. Global water resources and the role of groundwater in a resilient water future. Nat Rev Earth Environ 4, 87–101, doi:10.1038/s43017-022-00378-6, 2023

Schaller, M. F. and Fan, Y.: River basins as groundwater exporters and importers: Implications for water cycle and climate modeling, Journal of Geophysical Research, 114(D4), D04103, doi: 10.1029/2008JD010636, 2009

https://doi.org/10.5194/egusphere-2025-2952
Preprint. Discussion started: 14 July 2025

Sutanudjaja, E. H., et al.: Large-scale groundwater modeling using global datasets: a test case for the Rhine-Meuse basin, Hydrology and Earth System Sciences, 15(9): 2913-2935. Doi: 10.5194/hess-15-2913-2011, 2011

Sutanudjaja, E. H., et al. 2018. PCR-GLOBWB 2: a 5 arcmin global hydrological and water resources model, Geosci. Model Dev., 11, 2429–2453, https://doi.org/10.5194/gmd-11-2429-2018, 2018.

UNESCO World Water Assessment Programme. *The United Nations World Water Development Report 2024: Water for Prosperity and Peace*. Paris: UNESCO Publishing, 2024. https://unesdoc.unesco.org/ark:/48223/pf0000388948

van Beek, L. P. H., Wada, Y., and Bierkens, M. F. P.: Global monthly water stress: 1. Water balance and water availability: GLOBAL MONTHLY WATER STRESS, 1, Water Resources Research, 47(7), doi: 10.1029/2010WR009791, 2011

Verkaik, J., Sutanudjaja, E. H., and Oude Essink, G. H. P. et al.: GLOBGM v1.0: a parallel implementation of a 30 arcsec PCR-GLOBWB-MODFLOW global-scale groundwater model, Geosci. Model Dev., 17, 275–300, doi: 10.5194/gmd-17-275-2024, 2024

Wada, Y., van Beek, L. P. H., and Viviroli, D., et al.: Global monthly water stress: 2. Water demand and severity of water stress, Water Resour. Res., 47, W07518, doi:10.1029/2010WR009792, 2011a

Wada, Y., van Beek, L. P. H., and Bierkens, M. F. P.: Modelling global water stress of the recent past: on the relative importance of trends in water demand and climate variability, Hydrol. Earth Syst. Sci., 15, 3785–3808, doi: 10.5194/hess-15-3785-2011, 2011b

Wada, Y., Wisser, D., and Bierkens, M. F. P.: Global modeling of withdrawal, allocation and consumptive use of surface water and groundwater resources, Earth System Dynamics, 5(1): 15-40. doi: 10.5194/esd-5-15-2014, 2014

Weedon, G. P., Balsamo, G., Bellouin, N., Gomes, S., Best, M. J., and Viterbo, P.: The WFDEI meteorological forcing data set: WATCH Forcing Data methodology applied to ERAInterim reanalysis data, Water Resour. Res., 50, 7505–7514, https://doi.org/10.1002/2014WR015638, 2014.

Yamazaki, D., Oki, T., and Kanae, S.: Deriving a global river network map and its sub-grid topographic characteristics from a fine-resolution flow direction map, Hydrol. Earth Syst. Sci., 13, 2241–2251, doi: 10.5194/hess-13-2241-2009, 2009

Yamazaki, D., Kanae, S., Kim, H., and Oki, T.: A physically based description of floodplain inundation dynamics in a global river routing model, Water Resources Research 47(4), 2010WR009726, doi: https://doi.org/10.1029/2010WR009726, 2011

Yamazaki, D., O'Loughlin, F., Trigg, M. A., et al.: Development of the Global Width Database for Large Rivers. Water Resources Research 50(4): 3467-3480, doi: 10.1002/2013WR014664, 2014

Yang, W., Long, D., Scanlon, B. R., et al.: Human Intervention Will Stabilize Groundwater Storage Across the North China Plain, Water Resources Research, 58(2): e2021WR030884, doi: 10.1029/2021WR030884, 2022

Zhou, Y., Befus,K.M., Sawyer, A.H., et al. Opportunities and Challenges in Computing Fresh Groundwater Discharge to Continental Coastlines: A Multimodel Comparison for the United States Gulf and Atlantic Coasts. Water Resources Research. 54(10): 8363-8380, doi: 10.1029/2018WR023126, 2018